extinguishing metaflammation: mechanisms and therapeutic opportunities for immunological control of metabolic dysfunctions

Zande, H.J.P van der

CHAPTER 3

Soluble mannose receptor induces proinflammatory macrophage activation and metaflammation

Maria Embgenbroich[#], **Hendrik J.P. van der Zande**[#], Leonie Hussaarts[#], Jonas Schulte-Schrepping, Leonard R. Pelgrom, Noemí García-Tardón, Laura Schlautmann, Isabel Stoetzel, Kristian Händler, Joost M. Lambooij, Anna Zawistowska-Deniziak, Lisa Hoving, Karin de Ruiter, Marjolein Wijngaarden, Hanno Pijl, Ko Willems van Dijk, Bart Everts, Vanessa van Harmelen, Maria Yazdanbakhsh, Joachim L. Schultze, Bruno Guigas*, Sven Burgdorf*

[#]These authors contributed equally to this study
*These authors contributed equally to this study

PNAS. 118(31):e2103304118. (2021)
PMID: 34326259
doi: 10.1073/pnas.2103304118

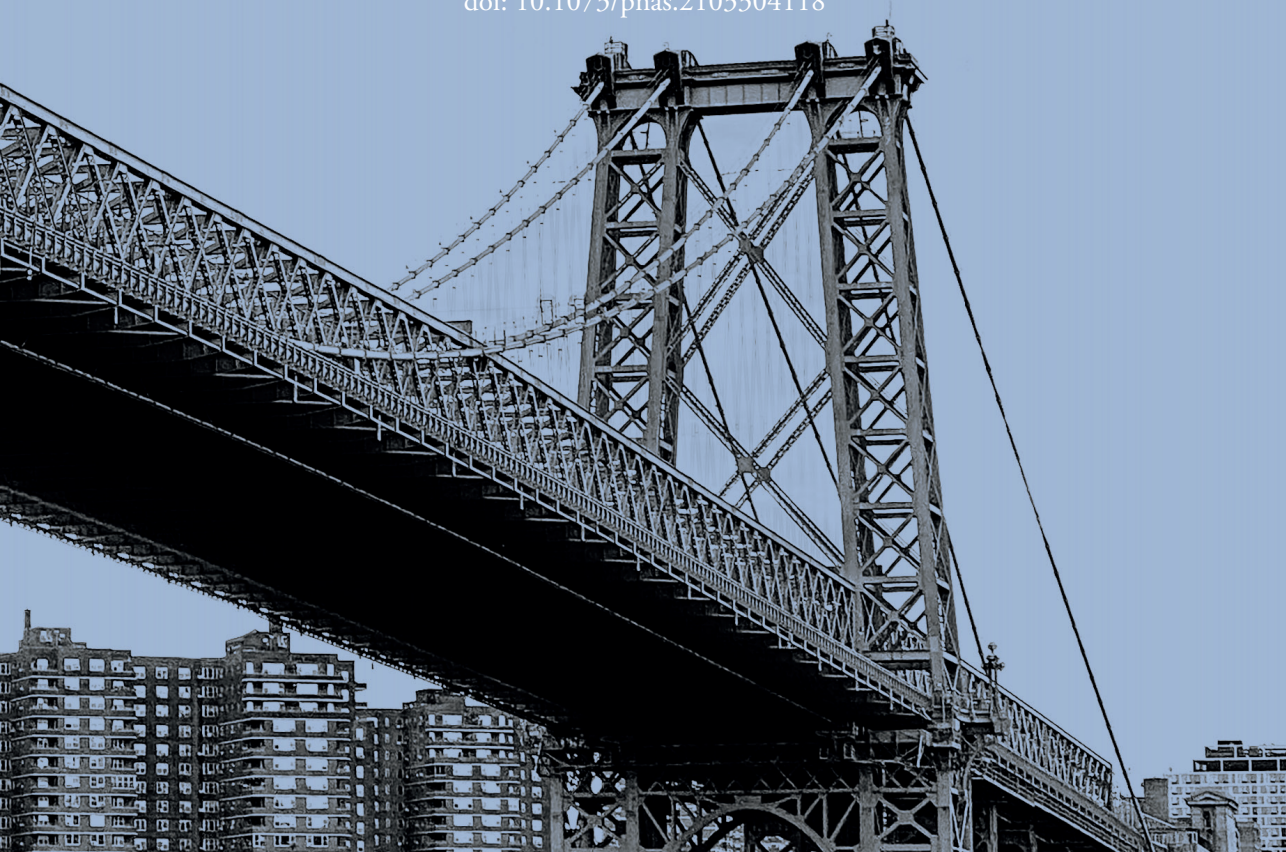

Abstract

Proinflammatory activation of macrophages in metabolic tissues is critically important in the induction of obesity-induced metaflammation. Here, we demonstrate that the soluble mannose receptor (sMR) plays a direct, functional role in both macrophage activation and metaflammation. We show that sMR binds CD45 on macrophages and inhibits its phosphatase activity, leading to a Src/Akt/NF-κB-mediated cellular reprogramming toward an inflammatory phenotype both *in vitro* and *in vivo*. Remarkably, increased serum sMR levels were observed in obese mice and humans and directly correlated with body weight. Importantly, enhanced sMR levels increase serum proinflammatory cytokines, activate tissue macrophages and promote insulin resistance. Altogether, our results reveal sMR as regulator of proinflammatory macrophage activation, which could constitute a therapeutic target for metaflammation and other hyperinflammatory diseases.

Introduction

Metaflammation defines a chronic inflammatory state in response to prolonged excessive nutrient intake and is characterized by low-grade inflammation of metabolic tissues (1). Macrophage reprogramming toward an inflammatory phenotype plays a critical role in obesity-induced metaflammation (2, 3). In lean individuals, macrophages in metabolic tissues maintain tissue homeostasis and insulin sensitivity, potentially through secreting anti-inflammatory cytokines, for example, TGF-b and IL-10 (1). In metaflammation, however, macrophages in adipose tissue and liver are activated through proinflammatory factors in their microenvironment, such as high levels of saturated free fatty acids (FA) and IFN-γ. Consequently, these macrophages produce high amounts of tumor necrosis factor (TNF), which directly inhibits canonical insulin signaling (4), leading to ectopic fat deposition in the liver and in skeletal muscles (5). Additionally, activation of Kupffer cells (KCs), the liver-resident macrophages, promotes recruitment and activation of inflammatory monocytes, which contribute to hepatic insulin resistance and steatosis (6-8).

The MR (also termed CD206) is a type I transmembrane protein belonging to the C-type lectin family, which is mainly expressed by subpopulations of macrophages, dendritic cells and endothelial cells (9, 10). The MR consists of a cysteine-rich region, a fibronectin type II domain, eight C-type lectin-like domains (CTLDs), a transmembrane region and a short cytosolic tail. Due to its high affinity for glycosylated antigens, the MR plays an important role in antigen uptake and presentation (11, 12). In addition to its functions as a transmembrane protein, the extracellular part of the MR can be shed by metalloproteases and released into the extracellular space (13, 14). Hence, soluble MR (sMR) can be detected in murine and human serum, and its level was found to be increased in patients with a variety of inflammatory diseases (15-20), correlating with severity of disease and even mortality. However, a physiological role of the sMR has not been studied yet, and it remains unclear whether the sMR can actively trigger inflammation.

Here, we report that sMR enhances macrophage proinflammatory activation, both *in vitro* and *in vivo*, and promotes metaflammation. We demonstrate that the sMR directly interacts with CD45 on the surface of macrophages and inhibits its phosphatase activity, leading to Src/Akt/NF-κB-mediated cellular reprogramming toward an inflammatory phenotype. Additionally, we found enhanced sMR serum levels in obese mice and humans and show that sMR-induced activation of macrophages triggers metaflammation *in vivo*.

Results

Soluble MR enhances proinflammatory cytokine secretion by macrophages

To investigate whether the MR is involved in the proinflammatory activation of macrophages, we first stimulated bone marrow-derived macrophages from wild-type or MR-deficient mice

with LPS. We found increased secretion of the proinflammatory cytokines TNF, IL-6, IL-1β and IL-12 in MR-expressing wild-type macrophages (Figure 1A). Because the MR itself lacks intracellular signaling motifs and hence no MR-mediated signaling has been described so far, we hypothesized that the sMR, resulting from the shedding of the MR extracellular region (Supplementary Figure 1A), might play a role in macrophage activation through direct interaction with macrophage surface proteins. To investigate this hypothesis, we generated a fusion protein consisting of the Fc region of human IgG1 and the extracellular region of the MR (encompassing the cysteine-rich region, the fibronectin region, and CTLD1-2) (FcMR) (21). We showed that treatment of MR-deficient macrophages with FcMR also enhanced proinflammatory cytokine secretion after LPS stimulation compared to isotype control-treated cells (Figure 1B). We observed similar results when treating MR-deficient macrophages with commercially available recombinant MR protein, consisting of the complete extracellular region of the protein (Figure 1C), suggesting that binding of sMR to the macrophage surface might indeed be responsible for the observed effects. To definitively prove that the sMR causes the observed increase in cytokine production, we purified sMR from the supernatant of MR-expressing macrophages (Supplementary Figure 1B) and showed that its administration to MR-deficient macrophages increased the secretion of TNF after LPS stimulation (Supplementary Figure 1C). Similar results were obtained from FcMR-treated primary macrophages isolated from murine liver, spleen or peritoneal cavity (Figure 1D), and in human monocyte-derived macrophages (moMϕ) after addition of recombinant human MR (Figure 1E) or after small interfering RNA (siRNA)-mediated down-regulation of the MR (Figure 1F). Interestingly, sMR also promoted a shift in cellular energy metabolism toward increased glycolysis in both murine and human macrophages (Supplementary Figure 1D-E), a bioenergetic hallmark of proinflammatory activation in macrophages (22, 23). Taken together, these data demonstrate that the sMR enhances proinflammatory activation of both murine and human macrophages.

sMR induces a proinflammatory phenotype in macrophages

To further dissect the effect of the sMR on macrophages, we treated MR-deficient macrophages with FcMR for 4, 12 or 24 h and performed RNA sequencing (RNA-seq) analysis (Figure 2A). Principle component analysis (PCA) revealed clear transcriptomic distinction of the samples in all analyzed conditions (Figure 2B). A heatmap of the 1,366 differentially expressed (DE) genes between FcMR treatment and control presented the substantial changes in gene expression due to the FcMR treatment over time with overlapping and unique gene sets (Figure 2C, Supplementary Figure 2A). Gene ontology enrichment analysis based on these shared and specific DE gene sets up-regulated upon FcMR treatment clearly confirmed inflammatory activation of macrophages (Supplementary Figure 2B).

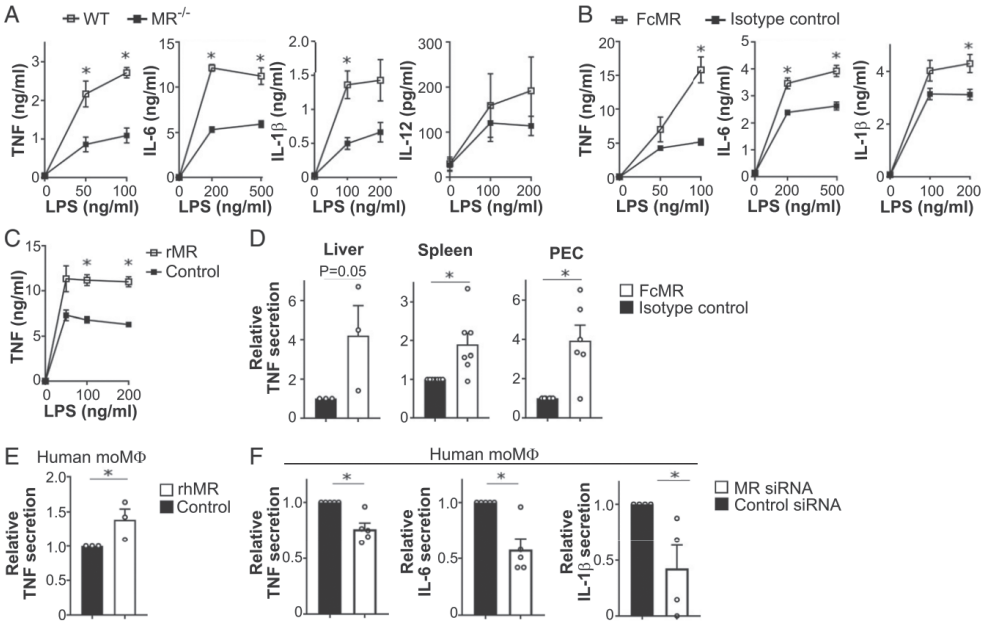

Figure 1: sMR induces proinflammatory cytokine secretion by macrophages. (A) Secretion of TNF, IL-6, IL-1β, and IL-12 by LPS-treated WT or MR-deficient ($MR^{-/-}$) macrophages. **(B)** TNF, IL-6, and IL-1β secretion by LPS-treated MR-deficient macrophages after incubation with FcMR. **(C)** Secretion of TNF by LPS-stimulated MR-deficient macrophages after addition of 0.3 μg/mL recombinant murine MR (rMR). **(D)** Primary murine macrophages were isolated from liver, spleen, or peritoneal cavity (PEC) of WT mice by magnetic separation of $F4/80^{+}$ cells. Secretion of TNF after LPS treatment and stimulation with FcMR were determined by ELISA. **(E)** Secretion of TNF by LPS-treated human monocyte-derived macrophages (moMΦ) after stimulation with 0.3 μg/mL recombinant human MR (rhMR). **(F)** Secretion of TNF, IL-6, and IL-1β by LPS-stimulated human moMΦ after siRNA-mediated down-regulation of the MR. All graphs are depicted as mean ± SEM; for all experiments, $n \geq 3$. *$P < 0.05$

The most significantly up-regulated genes in response to FcMR treatment further emphasized the strong and dynamic proinflammatory activation of macrophages, with well-known immunological key mediators such as TNF, IL-6, IL-1b, and IL-12 (Figure 2D, Supplementary Figure 2C). To classify the response elicited by sMR within the broad spectrum of macrophage activation phenotypes, we performed an enrichment analysis using macrophage activation signatures derived from our previous study comprising macrophages treated with 28 different immunological stimuli (24) and the gene sets of FcMR-mediated up-regulated genes per time point. This analysis revealed a striking similarity of FcMR-induced expression patterns to macrophage signatures associated with a chronic inflammatory phenotype, as induced by TNF, PGE2, and P3C (TPP) in our previous stimulation study (Figure 2E, Supplementary Figure 2D), further substantiating that the sMR reprograms macrophages toward a proinflammatory phenotype.

sMR activates macrophages by binding and inhibiting CD45

Next, we investigated the molecular mechanisms regulating sMR-induced macrophage reprogramming and searched for binding partners of the MR on the macrophage surface. To this end, we isolated cell lysates from macrophages that previously underwent surface biotinylation and performed immunoprecipitation using FcMR. Western blot analysis using streptavidin allowed us to monitor cell surface proteins interacting with sMR, including a clear band at the molecular weight of the phosphatase CD45 (between 180 and 220 kDa, depending on the splice variant; Supplementary Figure 3A), a known binding partner of the MR (25). Indeed, coimmunoprecipitation experiments revealed a physical interaction between the MR and CD45 on macrophages (Figure 3A-B).

CD45 can be expressed as different isoforms, depending on alternative splicing of its three exons A, B, and C. To identify the CD45 isoform interacting with sMR, we assessed their respective expression using isoform-specific antibodies. Analysis by Western blot and flow cytometry clearly showed the absence of exons A, B, and C in bone marrow-derived macrophages (Supplementary Figure 3B), pointing out that these cells only express the CD45RO isoform. This is in accordance with our RNA-seq data, which showed a specific read coverage of all exons of *Cd45* except for exons A, B, and C (Supplementary Figure 3C). Additionally, we showed that primary macrophages from spleen, white adipose tissue (WAT), liver, and the peritoneal cavity also expressed the CD45RO isoform (Supplementary Figure 3D), which is in agreement with previous literature (26). Accordingly, we confirmed the direct interaction of FcMR with CD45RO from primary splenic macrophages by far Western blot (Supplementary Figure 3E).

Since little is known about CD45 phosphatase activity in macrophages, we next investigated whether CD45 is active in these cells. Therefore, we immunoprecipitated CD45 from macrophage lysates and added 4-nitrophenyl phosphate (pNPP), from which dephosphorylation by CD45 can be quantified using colorimetry. We monitored a clear phosphatase activity, which was blocked by a CD45-specific inhibitor (Supplementary Figure 3F), demonstrating the presence of active CD45 in macrophages. Next, we tested the effect of sMR on CD45 phosphatase activity. To this end, we immunoprecipitated CD45 from lysates of FcMR-treated macrophages and showed that dephosphorylation of pNPP was reduced when compared to isotype control-treated cells (Figure 3C), indicating that the MR inhibited CD45 phosphatase activity. In a second approach, we assessed the dephosphorylation of a synthetic peptide containing pY505 of Lck, a specific substrate of CD45. We showed that preincubation of macrophages with FcMR increased pY505 phosphorylation (Figure 3D), confirming the inhibitory effect of the MR on CD45 phosphatase activity.

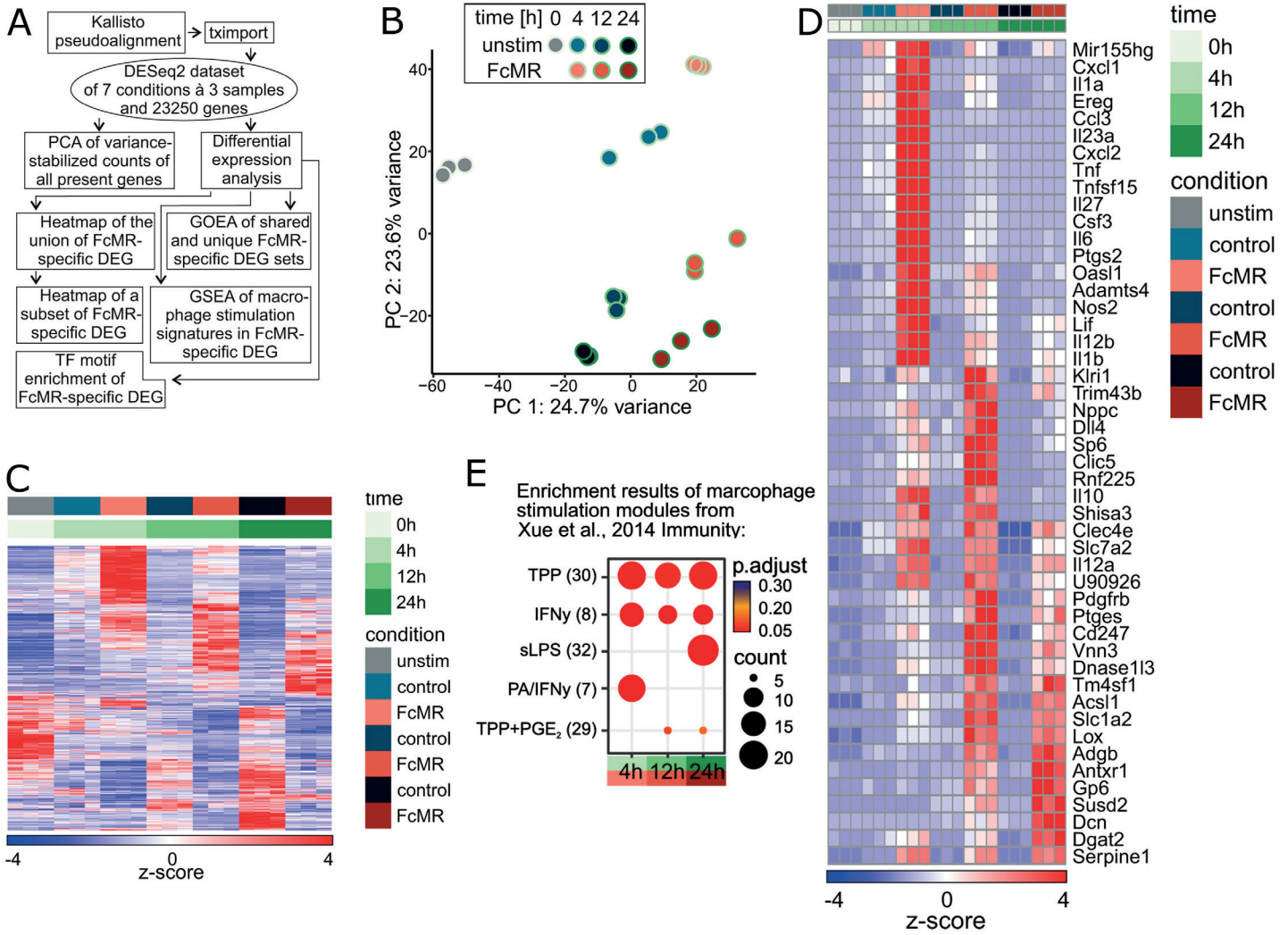
A
Kallisto pseudoalignment
tximport
DESeq2 dataset of 7 conditions à 3 samples and 23250 genes
PCA of variance-stabilized counts of all present genes
Differential expression analysis
Heatmap of the union of FcMR-specific DEG
GOEA of shared and unique FcMR-specific DEG sets
Heatmap of a subset of FcMR-specific DEG
GSEA of macrophage stimulation signatures in FcMR-specific DEG
TF motif enrichment of FcMR-specific DEG
B
time [h] 0 4 12 24
unstim
FcMR
PC 2: 23.6% variance
PC 1: 24.7% variance
C
time
0h
4h
12h
24h
condition
unstim
control
FcMR
control
FcMR
control
FcMR
-4
0
4
z-score
D
time
0h
4h
12h
24h
condition
unstim
control
FcMR
control
FcMR
control
FcMR
Mir155hg
Cxcl1
Il1a
Ereg
Ccl3
Il23a
Cxcl2
Tnf
Tnfsf15
Il27
Csf3
Il6
Ptgs2
Oasl1
Adamts4
Nos2
Lif
Il12b
Il1b
Klri1
Trim43b
Nppc
Dll4
Sp6
Clic5
Rnf225
Il10
Shisa3
Clec4e
Slc7a2
Il12a
U90926
Pdgfrb
Ptges
Cd247
Vnn3
Dnase1l3
Tm4sf1
Acsl1
Slc1a2
Lox
Adgb
Antxr1
Gp6
Susd2
Dcn
Dgat2
Serpine1
-4
0
4
z-score
E
Enrichment results of marcophage stimulation modules from Xue et al., 2014 Immunity:
TPP (30)
IFNγ (8)
sLPS (32)
PA/IFNγ (7)
TPP+PGE2 (29)
4h
12h
24h
p.adjust
0.30
0.20
0.05
count
5
10
15
20

▲Figure 2. Legend

Figure 2: RNAseq analysis identifies a proinflammatory phenotype in MR-treated macrophages. (**A**) Schematic overview of the bioinformatics RNA-seq analysis strategy. (**B**) Principal component analysis based on variance-stabilized counts of all 23,250 present genes. (**C**) Heatmap of hierarchically clustered, normalized, and z-scaled expression values of the union of 1,366 DE genes between FcMR-treated and control samples. (**D**) Normalized and z-scaled expression values of the union of the top 25 DE genes of each time point significantly up-regulated in at least two consecutive time points ranked according to their FcMR vs control samples visualized in a heatmap. (**E**) Dot plot of gene set enrichment analysis results of 49 predefined stimulus-specific macrophage expression signatures comprising 28 different stimuli on the FcMR-specific DE genes for each time point. TPP: TNF, PGE2, and Pam3Cys; PA: palmitic acid.

To investigate whether sMR-mediated inhibition of CD45 phosphatase activity plays a role in macrophage activation, we down-regulated CD45 expression using siRNA (Supplementary Figure 3G). Similar to inhibition of CD45 by sMR, CD45 down-regulation resulted in increased expression of TNF, IL-6, IL-1β and IL-12 after stimulation with LPS (Figure 3E). Importantly, addition of FcMR after down-regulating CD45 had no further effect on cytokine secretion (Figure 3F), demonstrating that the activating effect of the MR on macrophages was indeed due to its inhibition of CD45.

sMR-mediated inhibition of CD45 activates a Src/Akt/NF-κB signaling cascade in macrophages

We next investigated how sMR-mediated inhibition of CD45 results in macrophage reprogramming toward a proinflammatory phenotype. First, we screened for overrepresented transcription factor (TF) binding motifs in the nonprotein coding regions of FcMR-specific up-regulated DE genes. Network visualization of enriched TF binding motifs and their potential target DE genes clearly exposed NF-κB as the dominating transcriptional regulator of differential gene expression across all three time points (Figure 4A). In fact, from 351 known NF-κB target genes, 118 genes (34%) were significantly DE after FcMR treatment on at least one time point (Supplementary Figure 4A-B, Supplementary Dataset 1). Moreover, from all 351 NF-κB target genes, only 269 genes displayed a clear expression (BaseMean expression value ≥ 10) in macrophages, of which 117 genes (43%) were increased by FcMR. This proportion even increased up to 49% for all target genes with BaseMean expression value ≥ 1,000 (61 out of 124 target genes), suggesting a clear activation of NF-κB by the sMR. Indeed, macrophage treatment with FcMR significantly downregulated IkBa (Figure 4B), an inhibitor of NF-κB, which disables its nuclear translocation retaining NF-κB in the cytosol. Accordingly, enhanced nuclear translocation of both NF-κB subunits p65 and p50

(Figure 4C) and increased recruitment of p65 toward the TNF promotor (Supplementary Figure 4D) were observed after treatment with FcMR.

Subsequently, we aimed at identifying the signaling cascade leading from FcMR-mediated inhibition of CD45 to activation of NF-κB. Since CD45 can lead to the activation of Src kinases (27), Src in turn can activate Akt (28), and both Src and Akt have been associated with NF-κB activation (29-32), we investigated whether FcMR-mediated inhibition of CD45 resulted in NF-κB activation through signaling via Src and Akt. Indeed, FcMR treatment increased phosphorylation and hence activation of Src (Figure 4D). Furthermore, blocking Src using three different chemical inhibitors (PP2, KX2-391 and A419259) markedly decreased TNF secretion (Figure 4E). Of note, the effect of FcMR on TNF secretion was abolished in the presence of these Src inhibitors (Figure 4F), demonstrating that FcMR-induced macrophage activation depends on Src signaling. Similarly, FcMR treatment clearly increased phosphorylation of Akt (Figure 4G) and addition of an Akt-specific inhibitor decreased LPS-induced secretion of TNF, IL-6 and IL-1β (Figure 4H). Also here, the stimulatory effect of FcMR on cytokine secretion was abolished by Akt inhibition (Figure 4I), showing an important role for Akt signaling in FcMR-enhanced TNF secretion. Accordingly, inhibition of Akt prevented FcMR-induced translocation of NF-κB into the nucleus (Supplementary Figure 4D).

Taken together, these data demonstrate that sMR-mediated inhibition of CD45 results in activation of a Src/Akt signaling pathway leading to nuclear translocation of NF-κB and macrophage reprogramming toward an inflammatory phenotype.

Serum sMR is up-regulated in obesity and promotes high-fat diet-induced metabolic dysfunctions and hepatic steatosis

Next, we monitored whether the inflammatory effect of the MR on macrophages regulates inflammatory processes *in vivo* using a murine model of obesity-induced metaflammation. We first investigated whether high fat diet (HFD) feeding resulted in changes in serum sMR levels (Supplementary Figure 5A) and we demonstrated significantly increased sMR concentrations in the serum of HFD-fed obese mice, as compared to lean control diet (CD)-fed mice (Figure 5A). Additionally, serum sMR levels positively correlated with body weight and fat mass of the mice (Figures 5B-C). In humans, serum sMR levels were also increased in obese individuals when compared to lean subjects (Figure 5D) and correlated positively with body mass index and fat mass (Figures 5E-F), indicating a direct correlation between serum sMR levels and obesity in both humans and mice.

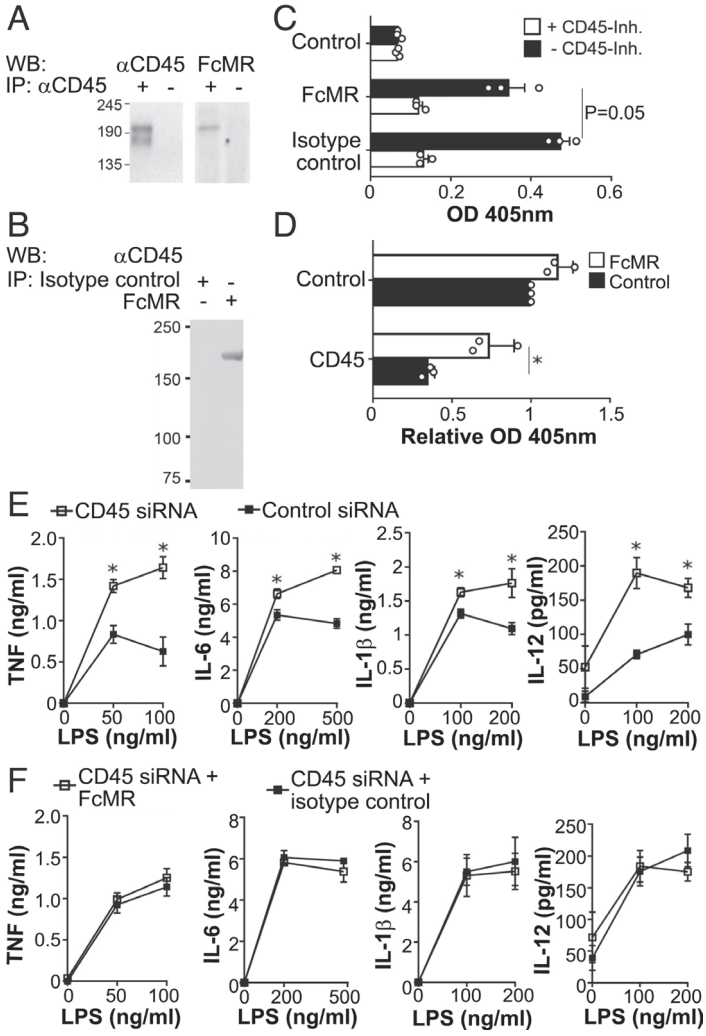

Figure 3: MR inhibits phosphatase activity of CD45 on macrophages. (**A**) Macrophage cell lysates were immune precipitated using a CD45-specific and body and stained for FcMR binding by far Western blot. (**B**) Macrophage lysates were immune precipitated with FcMR or isotype control and stained for CD45 by Western blot. (**C**) CD45 was precipitated from lysates of FcMR- or isotype control-treated macrophages and incubated with 4-NPP in the presence or absence of the CD45 inhibitor SF1670. Graph depicts CD45-mediated dephosphorylation of 4-NPP measured by colorimetry. Samples precipitated without CD45 antibody were used as controls. (**D**) CD45 was precipitated from lysates of FcMR- or isotype control-treated macrophages and incubated with the CD45 substrate TATEGQ-pY-QPQ. Graph depicts the phosphorylation status of TATEGQ-pY-QPQ. Samples precipitated without CD45 antibody were used as controls. (**E**) Secretion of TNF, IL-6, IL-1β, and IL-12 by LPS-stimulated macrophages after siRNA-mediated down-regulation of CD45. (**F**) Influence of FcMR on secretion of TNF, IL-6, IL-1β, and IL-12 by LPS-stimulated macrophages after siRNA-mediated down-regulation of CD45. All graphs are depicted as mean ± SEM; for all experiments, n ≥ 3. *$P < 0.05$.

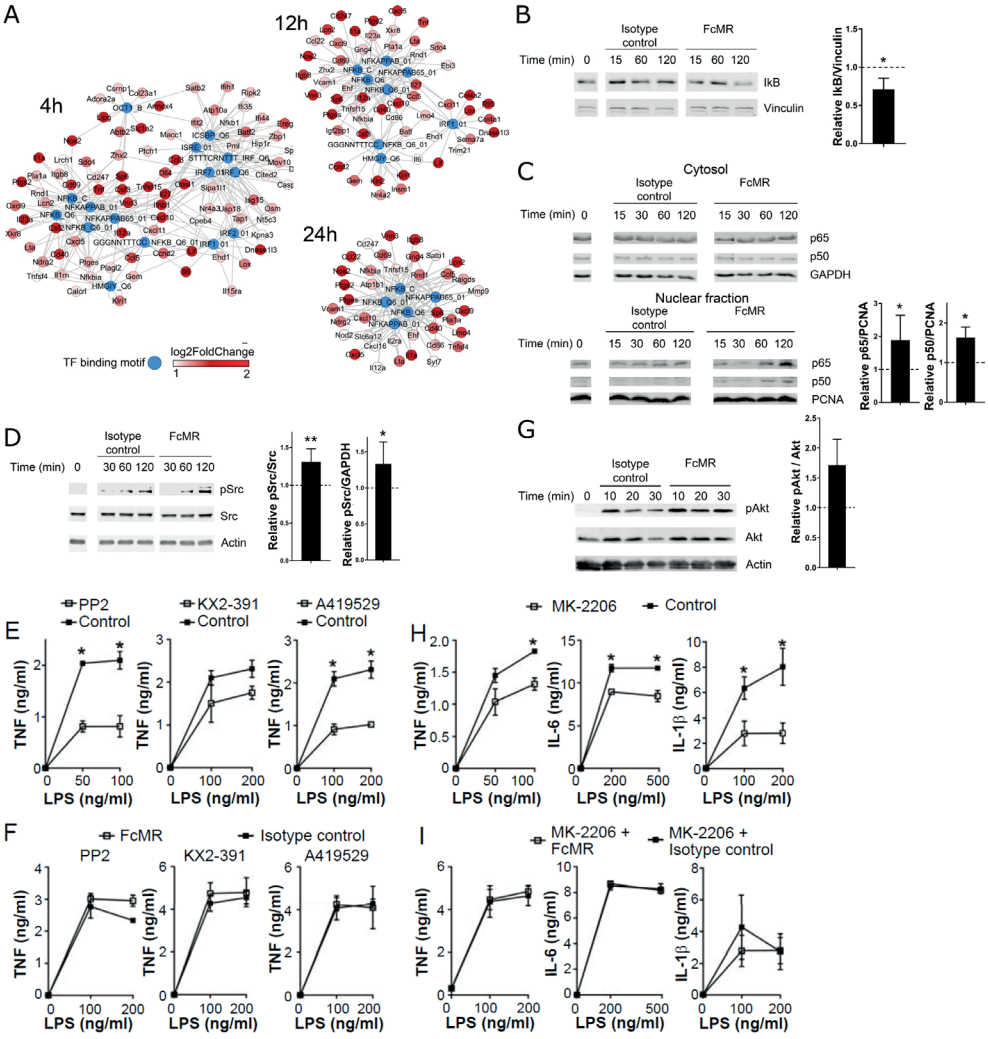

Figure 4: MR reprograms macrophages to a proinflammatory phenotype via Src/Akt/NF-κB signaling. (**A**) Network visualization of significantly enriched (q-value < 0.1) TF binding motifs (blue) of the MSigDB motif gene set and their potential targets (colored in red according to their FC) among the up-regulated DE genes after 4, 12, or 24 h of FcMR treatment. (**B**) MR-deficient macrophages were treated with FcMR or isotype control. Total IκB was determined by Western blot. (**C**) MR-deficient macrophages were treated with FcMR or isotype control. p65 and p50 were monitored in the cytosolic and nuclear fraction by Western blot. (**D**) MR-deficient macrophages were treated with FcMR or isotype control. Src and phosphorylated Src (pSrc) were determined by Western blot. (**E**) MR-deficient macrophages were treated with 3 mM PP2, 1 mM KX2-391, or 1 mM A419529 and stimulated with LPS. TNF secretion was monitored by ELISA. (**F**) FcMR or isotype control-treated MR-deficient macrophages were incubated with PP2, KX2-391, or A419259 and stimulated with LPS. Secretion of TNF was determined by ELISA. (**G**) MR-deficient macrophages

▲Figure 4. Legend

were treated with FcMR or isotype control for 30 min. Akt and phosphorylated Akt (pAkt) were determined by Western blot. (**H**) MR-deficient macrophages were treated with 5 mM MK-2206 and stimulated with LPS. TNF, IL-6, and IL-1β secretion was monitored by ELISA. (**I**) FcMR or isotype control-treated MR-deficient macrophages were incubated with MK-2206 and stimulated with LPS. Secretion of TNF, IL-6, and IL-1β was determined by ELISA. All graphs are depicted as mean ± SEM; for all experiments, n ≥ 3. $*P < 0.05$.

Subsequently, we analyzed changes in MR-expressing cells as putative source for increased sMR serum levels in HFD-fed mice. In spleen and WAT of both CD- and HFD-fed mice, nearly all MR-expressing cells were $CD45^+$, whereas in liver, $CD45^-$ cells also expressed the MR. These latter cells were identified as $CD31^+CD146^+$ liver sinusoidal endothelial cells (LSECs), which were indeed previously reported to express the MR (9). Importantly, whereas no differences in MR expression could be detected in $CD45^-$ cells, a clear increase in MR^+ cells was observed in $CD45^+$ hematopoietic cells in spleen, liver and WAT of HFD-fed obese mice compared to CD-fed mice (Figure 5G). Of note, $CD45^+MR^+$ cells in all three organs were mainly identified as $CD64^+F4/80^+$ macrophages (Supplementary Figure 5B-C). Taken together, this demonstrates that obesity increased MR-expressing macrophages in spleen, liver and WAT.

To test whether increased sMR levels regulate macrophage-mediated inflammatory diseases *in vivo*, we then analyzed the development of obesity-induced metaflammation in MR-deficient mice (Figure 6A). Whereas no differences in body weights were found between wild-type and MR-deficient mice on CD, MR-deficient mice gained slightly less weight on HFD (Figure 6B). This effect was not due to a decrease in caloric intake, as HFD-fed $MR^{-/-}$ mice rather displayed a mild increase in food consumption when compared to WT mice (Supplementary Figure 6A). Furthermore, the HFD-induced reductions in locomotor activity, energy expenditure, and carbohydrate oxidation observed in WT obese mice were found to be partly reverted in $MR^{-/-}$ mice (Supplementary Figure 6B-E). Analysis of body composition showed that the lower body weight in HFD-fed MR-deficient mice resulted exclusively from a reduction in fat mass, without affecting lean mass (Figure 6C). Accordingly, the weights of epididymal, mesenteric and subcutaneous (inguinal) WAT, as well as brown adipose tissue (BAT), were lower in HFD-fed MR-deficient mice (Supplementary Figure 7A-B). This decrease in WAT mass in HFD-fed $MR^{-/-}$ mice appears to be due to reduced adipocyte hyperplasia rather than hypertrophy (Supplementary Figure 8A-E). Of note, no significant differences between genotypes were observed in gene expression of proteins involved in adipocyte differentiation and FA metabolism in epididymal white adipose tissue (eWAT; Supplementary Figure 8F) nor in beiging or thermogenic markers in

inguinal white adipose tissue (iWAT) and BAT, respectively (Supplementary Figure 8G-H). Liver weight was also markedly lower in HFD-fed MR-deficient mice as compared to wild-type controls (Figure 6D), suggesting a reduction in hepatic steatosis. Indeed, MR-deficient mice were completely protected against HFD-induced hepatic steatosis (Figure 6F-G). Accordingly, hepatic triglycerides, total cholesterol and phospholipids contents (Figure 6H, Supplementary Figure 7F), and hepatic gene expression of lipid droplet-associated proteins (Supplementary Figure 7H) were markedly lower in HFD-fed $MR^{-/-}$ mice. Furthermore, the expression of various genes encoding proteins involved in FA transport and storage were significantly decreased in HFD-fed $MR^{-/-}$ mice, whereas no changes in expression of genes implicated in FA oxidation were observed (Supplementary Figure 7I). Circulating alanine aminotransaminase (ALAT) levels were also markedly decreased in HFD-fed MR-deficient mice (Supplementary Figure 7G).

We next assessed metabolic consequences of MR deficiency. Although no differences in metabolic parameters were observed between genotypes in CD-fed mice, HFD-fed MR-deficient mice displayed lower fasting plasma insulin levels than wild-type mice, whereas fasting glucose levels were unchanged (Supplementary Figure 7C-D). The calculated Homeostasis Model Assessment of Insulin Resistance index was significantly reduced in HFD-fed MR-deficient mice (Figure 6E), suggesting that insulin resistance is less severe in these mice. In line with this, whole-body insulin sensitivity (Figure 6I) and glucose tolerance (Figure 6J) were higher, despite similar insulin levels (Supplementary Figure 7E), in HFD-fed MR-deficient mice compared to wild-type mice. Importantly, the alleviated hepatic steatosis and whole-body metabolic homeostasis were still observed when HFD-fed MR-deficient mice were weight-paired to their wild-type counterparts (Supplementary Figure 11A-D), indicating that MR deficiency protects against HFD-induced metabolic dysfunctions independently of body weight changes. Altogether, these data indicate that the MR might contribute to obesity-induced metabolic dysfunctions.

MR promotes inflammatory macrophage accumulation in eWAT and liver during obesity

Since our *in vitro* data demonstrate that the MR reprograms macrophages toward an inflammatory phenotype, we next investigated whether the observed metabolic changes in MR-deficient mice might be caused by reduced proinflammatory macrophage activation in metabolic tissues.

As previously reported, HFD significantly increased obesity-associated proinflammatory $CD11c^{+}$ adipose tissue macrophages (ATMs) in eWAT of wild-type mice (33), whereas total

ATMs and monocytes were not affected (Figures 6K-M, Supplementary Figure 9). Remarkably, while no significant differences in total ATMs and monocyte numbers were observed between genotypes, inflammatory CD11c$^+$ ATM numbers were found to be significantly higher in HFD-fed MR-expressing wild-type mice as compared to MR-deficient mice (Figure 6K-M), and strongly correlated with whole-body insulin resistance (Figure 6N).

In the liver, HFD significantly increased proinflammatory CD11c$^+$ KCs and monocytes in wild-type mice, while total KCs were not affected (Figure 6O-Q). Similar to what was observed in eWAT, inflammatory CD11c$^+$ KCs, but also monocytes, were more abundant in liver of MR-expressing wild-type mice as compared to MR-deficient mice, of which the CD11c$^+$ KCs again correlated strongly with insulin resistance (Figure 6R), while total KCs were not affected (Figure 6O-Q). This was associated with higher expression of genes involved in proinflammatory macrophage activation in liver and WAT of MR-expressing wild-type mice (Supplementary Figure 10B,D). Importantly, these differences in proinflammatory macrophage abundances in metabolic tissues were still present when wild-type and MR-deficient mice were weight-paired (Supplementary Figure 11E-F), indicating that also the regulation of obesity-induced proinflammatory macrophages by the MR is independent of changes in body weight. By contrast, MR deficiency neither affected other myeloid and lymphocyte subsets nor T cell-associated cytokines gene expression in eWAT or liver from HFD-fed mice (Supplementary Figure 10).

Taken together, these data provide first indications that the MR might contribute to obesity-induced metaflammation.

sMR treatment induces proinflammatory cytokines, metabolic dysfunctions, and increased proinflammatory macrophages

To univocally determine the role of the MR in metaflammation, we investigated whether *in vivo* administration of sMR in lean mice is able to induce macrophage activation and metabolic dysfunctions, by intraperitoneally injecting FcMR or isotype control every three days for four weeks (Figure 7A). We first monitored circulating cytokine levels in response to a single intraperitoneal injection of FcMR in CD-fed mice. In accordance with our *in vitro* experiments, even a single injection of FcMR acutely increased serum levels of TNF and IL-6 and the chemokine MCP-1/CCL2 compared to isotype control-treated mice (Figure 7B).

After four weeks of treatment, we monitored a mild increase in body weight in FcMR-treated mice compared to control mice (Figs. 7C-D). In addition, insulin sensitivity, as measured by an acute drop in blood glucose levels following insulin intraperitoneal (i.p.) injection, was reduced in FcMR-treated mice compared to control mice (Figs. 7E-F), confirming the detrimental effect of the sMR on whole-body metabolic homeostasis. Importantly, the effect

of FcMR on HFD-induced insulin resistance was even more pronounced when mice were fed an HFD concomitantly with FcMR treatment for four weeks, underlining the inflammatory effect of the sMR in mice fed an HFD (Supplementary Figure 12).

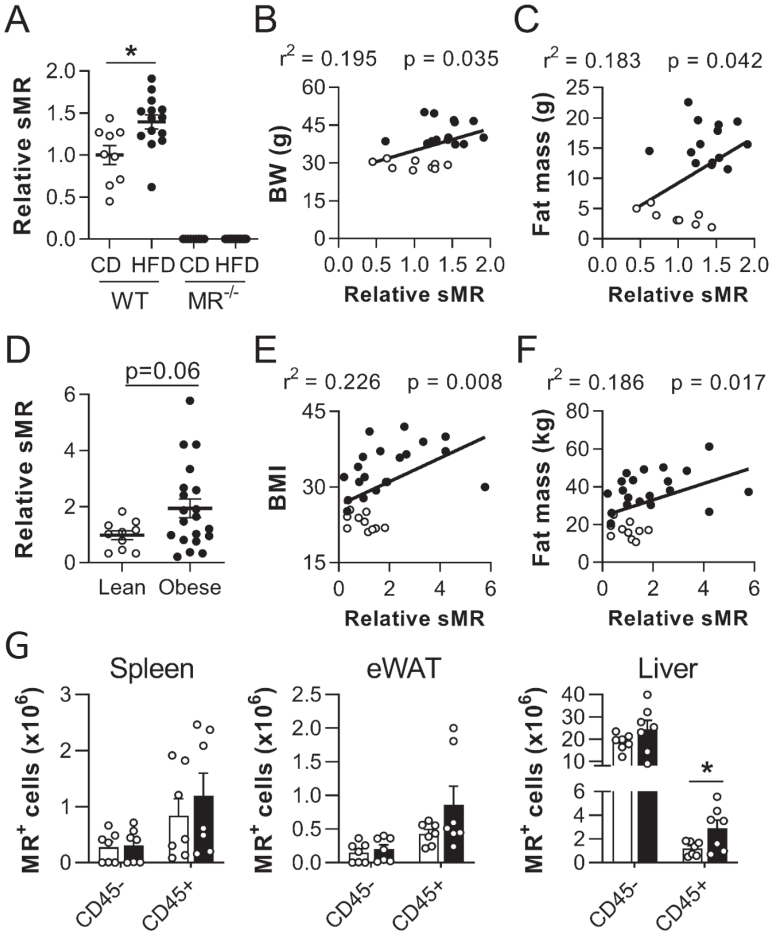

Figure 5: sMR is up-regulated in obesity. (**A**) sMR levels in the serum of wild-type or MR-deficient mice after HFD or CD feeding. (**B-C**) Correlation of sMR serum levels and body weight (*B*) or fat mass (*C*) of all mice depicted in *A*. (**D**) sMR levels in the serum of lean and obese humans. (**E-F**) Correlation between sMR serum levels and body mass index (*E*) or fat mass (*F*). (**G**) Wild-type mice were fed an HFD or CD for 18 weeks. MR-expressing cells were quantified in different organs. Results are expressed as means ± SEM; n=7 mice per group for G. *$P < 0.05$.

FcMR treatment increased macrophage numbers in eWAT of lean mice (Figure 7G). Moreover, gene expression of *Il1b, Tnf, Il6* and *Ccl2* was increased in eWAT of FcMR-treated

lean mice (Figure 7H). Accordingly, macrophages isolated from these mice showed increased secretion of most of these cytokines upon stimulation with LPS (Figure 7I), demonstrating that, in lean mice, increased serum sMR levels induce the secretion of proinflammatory cytokines, induce whole-body insulin resistance and promote macrophage activation in metabolic tissues *in vivo*.

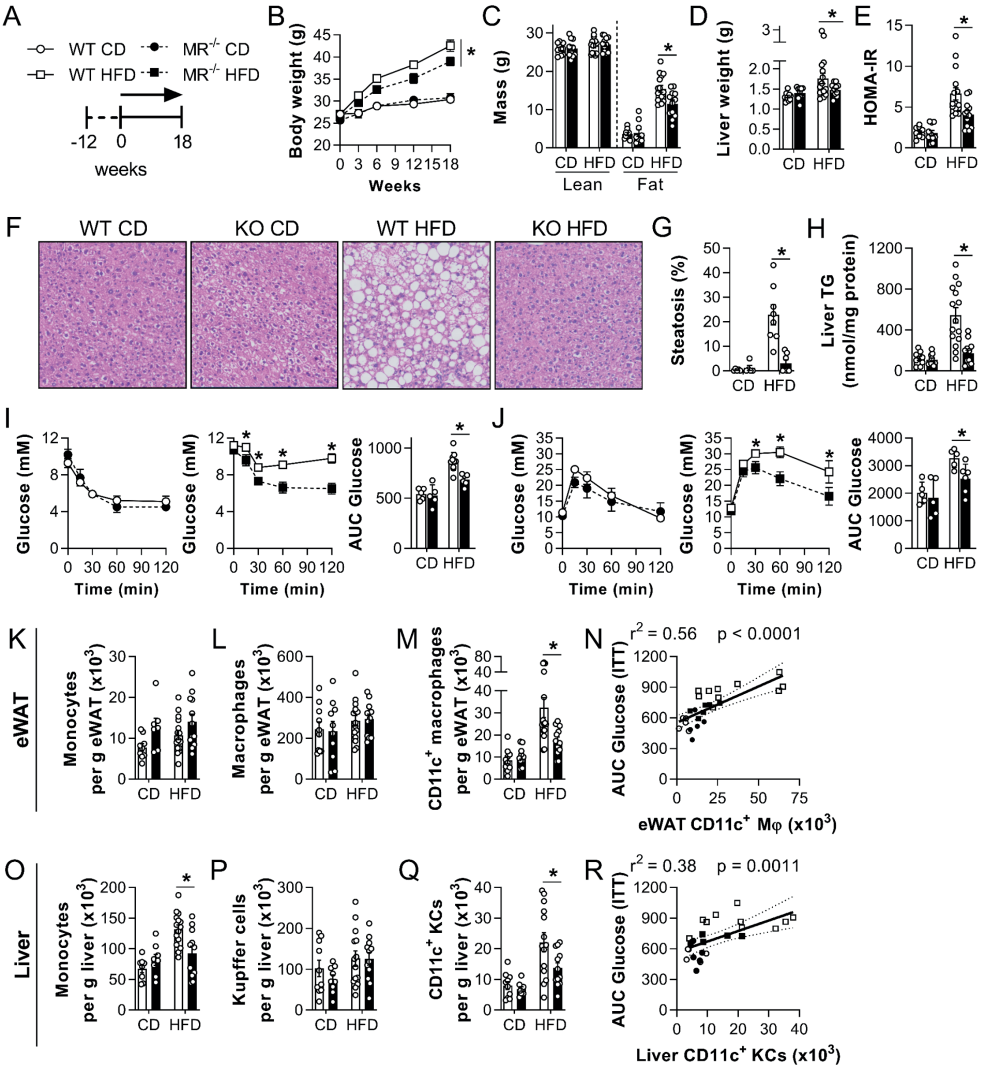

Figure 6: MR regulates WAT and liver macrophage activation, hepatic steatosis, and metabolic homeostasis after HFD feeding. (**A**) Wild-type (WT) and MR-deficient ($MR^{-/-}$) mice were fed an HFD or CD for 18 weeks. (**B**) Body weight of mice on diet for 18 weeks. (**C**) Lean and fat mass after

◀Figure 6. Legend (Continued)

18 weeks on diet determined by MRI. (**D**) Liver weight after 18 weeks on diet. (**E**) Homeostasis Model Assessment of Insulin Resistance index (HOMA-IR) based on blood glucose and fasting insulin. (**F-G**) Hematoxylin and eosin staining (*F*) and quantification (*G*) of hepatic steatosis. (**H**) Levels of liver triglycerides. (**I**) Intraperitoneal insulin tolerance test. Blood glucose levels were measured at the indicated time points, and the area under the curve (AUC) of the glucose excursion curve was calculated as a surrogate measure for whole-body insulin resistance. (**J**) Intraperitoneal glucose tolerance test. The AUC of the glucose excursion curve was calculated as a surrogate measure for whole-body glucose intolerance. (**K-M**) Numbers of total monocytes (*K*), macrophages (*L*), and CD11c$^+$ macrophages (*M*) per gram eWAT determined by flow cytometry. (**N**) Correlation between eWAT CD11c$^+$ macrophages and whole-body insulin resistance, assessed by the AUC of the glucose excursion curve. (**O-Q**) Numbers of total monocytes (*O*), KCs (*P*), and CD11c$^+$ KCs (*Q*) per gram liver determined by flow cytometry. (**R**) Correlation between CD11c$^+$ KCs and whole-body insulin resistance. Results are expressed as means ± SEM; n=5-15 mice per group. **P* <0.05.

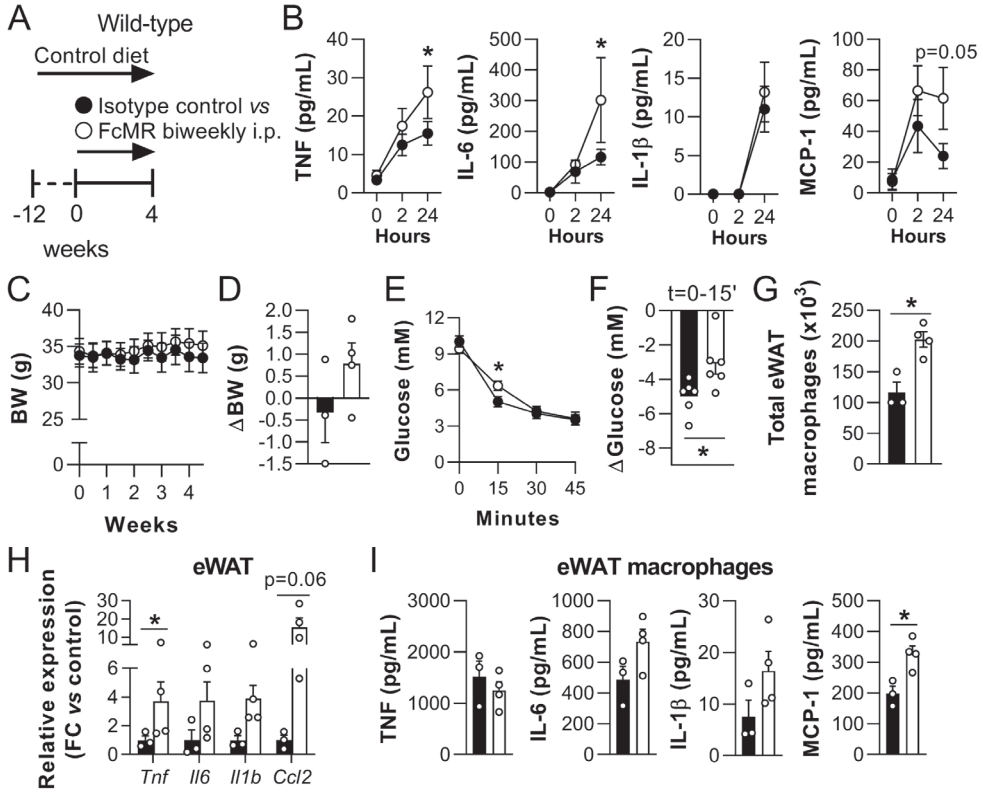

Figure 7: Increased MR levels regulate whole-body metabolism and promote inflammation. (**A**) CD-fed WT mice were injected i.p. with 4.82 μmoles/mouse FcMR or isotype control for 4 weeks. (**B**) Serum cytokine concentrations were determined by cytometric bead array (CBA) at the

▲Figure 7. Legend (Continued)

indicated timepoints post-first injection. (**C-D**) Graphs depicting body weight over time (*C*) and overall change in body weight (*D*). (**E-F**) Intraperitoneal insulin tolerance test after FcMR treatment of CD-fed mice. Changes in circulating glucose levels at 15 min post insulin i.p. (*F*). (**G**) The number of F4/80$^+$ magnetic cell separation (MACS)-sorted eWAT macrophages was determined after 4 weeks of treatment. (**H**) Expression of inflammatory genes in eWAT was monitored by qPCR. (**I**) Cytokine secretion by F4/80$^+$ macrophages from eWAT was determined by CBA after stimulation with 100 ng/ml LPS. BW: body weight. Results are expressed as means ± SEM; n=3-5 mice per group. *P <0.05.

Discussion

The MR as a member of the C-type lectin family has mainly been described as an endocytic receptor recognizing glycosylated antigens and mediating antigen processing and presentation (34, 35). However, the extracellular region of the MR can be shed by metalloproteases and released as a soluble protein in the extracellular space. Consequently, the sMR is detectable in murine and human serum (13, 14), and recent studies reported an increase of serum sMR levels in a variety of inflammatory diseases and serum sMR levels directly correlated with severity of disease and mortality (15-20). Here, we demonstrated that, in addition to a mere phenotypic correlation, the sMR plays a direct, functional role in macrophage activation, driving reprogramming toward a proinflammatory phenotype. By interacting with and inactivating CD45, the sMR reprograms macrophages via activation of Src/Akt signaling and nuclear translocation of NF-κB. *In vivo*, sMR levels were increased in obese mice and humans as compared to lean controls, and we found that MR deficiency reduced adipose tissue and liver proinflammatory macrophages and protected against obesity-induced metabolic dysfunctions. Consistently, treatment of lean mice with sMR acutely increased serum proinflammatory cytokines and induced both tissue macrophage activation and systemic insulin resistance.

Although wild-type (WT) and MR$^{-/-}$ mice on CD were phenotypically similar in term of body composition and whole-body metabolic homeostasis, MR$^{-/-}$ mice on HFD appeared to be slightly resistant to HFD-induced body weight gain and displayed markedly improved insulin sensitivity and glucose tolerance when compared to WT mice. However, it is important to underline that body weight pairing of obese mice from the two genotypes clearly indicated that the lower body weight observed in HFD-fed MR$^{-/-}$ mice only marginally contributed to their lower hepatic steatosis, improved whole-body metabolic homeostasis and phenotypic changes in AT and liver macrophages. In addition, we found that sMR injections promoted inflammation but only induced mild insulin resistance in lean WT mice. Although significant, this effect was modest and may be explained by several factors, including the timing of administration and dosage, but also by the fact

that lean mice are highly insulin sensitive. Of note, injecting sMR at the start of HFD feeding accelerated the development of insulin resistance, which supports a role for sMR in promoting metaflammation.

In this study, we found increased MR^+ cells in spleen, liver, and eWAT upon HFD feeding, which were almost exclusively macrophages. Since cell surface MR can be shed and released as a soluble form, obesity-induced changes in tissue homeostasis may increase MR expression and sMR release by macrophages, creating increased local and systemic sMR levels to promote macrophage-mediated inflammation and metabolic dysfunctions. An important factor in this process could be the ligand-inducible TF PPAR-γ, which is activated, among others, by free FAs. Indeed, single-cell RNA sequencing analysis of adipose tissue immune cells revealed that PPAR signaling is among the up-regulated pathways in obesity-induced lipid-associated macrophages in both mice and humans (36). Since *Mrc1* (encoding the MR) is also a direct target gene of PPAR-γ (37), obesity-induced activation of PPAR-γ in macrophages may lead to enhanced transcription of the MR, eventually resulting in increased sMR levels. One of the limitations of our study was the use of constitutive whole-body $MR^{-/-}$ mice instead of a myeloid cell-specific knockout model, which is currently not available. As such, the main cellular source of circulating proinflammatory sMR remains to be confirmed, although it is conceivable that a significant part of the increased circulating sMR during obesity may also be derived from non-myeloid MR-expressing cells, such as LSECs.

Our data demonstrate that macrophage activation by the MR was due to MR-mediated inhibition of CD45, which in turn leads to activation of Src and Akt, and nuclear translocation of NF-κB. CD45 has been postulated to inhibit Src kinases (27) and Akt (28), a known regulator of NF-κB (30, 31, 38). Here, we show that CD45-mediated dephosphorylation of Src induces Akt-mediated nuclear translocation of NF-κB, and that the sMR uses this signaling pathway to induce macrophage reprogramming toward an inflammatory phenotype. MR-mediated macrophage activation depended on Akt signaling, as its inhibition abrogated MR-mediated nuclear translocation of NF-κB and ensuing TNF and IL-6 secretion by macrophages. Additionally, Akt has been postulated as a regulator that can fine tune NF-κB-mediated responses through regulating efficient binding of p65 to specific target promoters (32). Of note, these authors demonstrated that NF-κB-mediated expression of TNF was particularly sensitive to Akt signaling, which is in accordance with the Akt-dependency of TNF expression after MR-induced activation of macrophages described here.

The immunometabolic phenotype of obese MR-deficient mice resembles that of mice deficient for MGL/CLEC10A, another member of the C-type lectin family. Indeed,

these mice displayed reduced hepatic steatosis, insulin resistance and glucose intolerance upon HFD when compared to wild-type mice, a feature that was associated with lower AT proinflammatory macrophages (39). In another context, MGL/CLEC10A was also shown to bind and inactivate CD45 (40), offering the possibility that MGL/CLEC10A can directly induce macrophage reprogramming by inhibition of CD45, similar to the MR. Future studies will have to reveal whether MGL/CLEC10A indeed plays a direct role in macrophage activation, whether its expression is also increased in HFD-induced obesity, and whether this may be mediated by a soluble form of MGL/CLEC10A.

In summary, we demonstrate that a soluble form of the MR reprograms macrophages toward an inflammatory phenotype by interacting with CD45 on the surface of these macrophages. MR-mediated inhibition of CD45 activated Src and Akt kinases, leading to nuclear translocation of NF-κB and induction of a transcriptional program that ultimately results in enhanced inflammatory cytokine production. Furthermore, sMR levels in serum of obese mice and humans are increased, strongly correlating with body weight and adiposity, a feature that needs however to be confirmed in female mice and larger population studies. Accordingly, MR deficiency resulted in fewer adipose tissue and liver proinflammatory macrophages and protection against hepatic steatosis and metaflammation, whereas increased MR levels induced elevated serum proinflammatory cytokines, macrophage activation and metabolic dysfunctions. Altogether, our results identify sMR as a regulator of proinflammatory macrophage activation and could contribute to the development of new therapeutic strategies for metaflammation and other hyperinflammatory diseases. Targeting MR-mediated activation of macrophages using antibodies, nanobodies, aptamers or small molecules that could prevent MR interacting with macrophage CD45RO might open new possibilities for therapeutics aimed at dampening (meta)inflammation.

Material and Methods

Antibodies and Reagents

A detailed list of antibodies and reagents is included in the Supplementary information.

Generation of bone marrow-derived macrophages

Bone marrow was flushed from the femurs and tibias of mice and cultured for 7 days in medium containing 2.5 % supernatant of a Granulocyte Macrophage Colony-Stimulating Factor (GM-CSF)-producing cell line (total concentration 150 ng/mL).

Generation and purification of FcMR

FcMR proteins (encompassing the CR region, the FN II domain and CTLD1-2 fused to the Fc region of hIgG1) and isotype controls (Fc region of hIgG1) were generated as described previously (21). For all *in vitro* experiments, FcMR and isotype controls were used in a concentration of 10 μg/mL.

Monitoring secretion of TNF, IL-6, IL-1β and IL-12

Macrophages were incubated with 10 μg/mL FcMR or isotype control, 300 ng/mL recombinant MR (2535-MM-050, R&D Systems), 30 ng/mL purified sMR, 3 μM PP2, 1 μM KX2-391, 1 μM A419259 or 5 μM MK-2206. After 2 h, LPS was added in the given concentrations. Unless indicated differently, supernatants were collected at 3 h (TNF) or 18 h (IL-6, IL-12p70) post-LPS stimulation. For secretion of IL-1β, cells were incubated with LPS for 3 h and with 10 mM nigericin for another 1 h. Secreted cytokine levels were measured by enzyme-linked immunosorbent assay (ELISA). Levels of TNF, IL-6, IL-1β, and MCP-1 in the circulation at 2 h post-FcMR, or isotype control injection, or in culture supernatant of LPS-treated eWAT macrophages were measured using the cytometric bead array kits (BD Biosciences), per manufacturer's recommendations.

Mice and diet

All animal experiments were performed in accordance with the Guide for the Care and Use of Laboratory Animals of the Institute for Laboratory Animal Research and have received approval from the university Ethical Review Boards (DEC No. 12199; Leiden University Medical Center, Leiden, The Netherlands). To reduce variation due to sex hormone cycles on whole-body metabolism, male mice were used for all *in vivo* experiments. $MR^{-/-}$ mice were generated on C57BL/6J background, regularly backcrossed to C57BL/6J, and compared to age-matched C57BL/6J wild-type mice from the same mouse facility. To minimize eventual effects of genotype-dependent microbiota differences on metabolic and immunological outcomes, the beddings of WT and $MR^{-/-}$ mice were frequently mixed before randomization. All mice were housed in a temperature-controlled room with a 12-hour light-dark cycle. Throughout the experiment, food and tap water were available ad libitum. The 8- to 10-weeks-old male mice were randomized according to total body weight, lean and fat mass, and fasting plasma glucose, insulin, TC and TG levels, after which they were fed an HFD (45% energy derived from fat, D12451, Research Diets) or a CD (10% energy derived from fat, D12450B, Research Diets) for 18 weeks. An *a priori* power calculation was done. Analysis was performed blinded to the conditions. For *in vivo* FcMR treatment,

C57BL/6J wild-type littermate mice were randomized as above. Subsequently, mice were biweekly intraperitoneally injected with 50 μg FcMR or 6.75 μg isotype control, to yield the same administered dose of hIgG1, for four weeks while either on CD or concomitant with the start of HFD feeding.

Quantification and statistical analysis

All data are presented as mean ± SEM. Statistical analysis was performed using GraphPad Prism 8.0 (GraphPad Software) with unpaired t-test, one-way or two-way ANOVA, followed by Fisher's post hoc test. Differences between groups were considered statistically significant at $P < 0.05$. Outliers were identified according to the two-SD method. Single data points represent mean values of distinct independent experiments (*in vitro*) or individual mice (*in vivo*).

Data and Software availability

The complete RNAseq analysis including code and count data can be found under jsschrepping/Embgenbroich_2020 at https://github.com/schultzelab. Additionally, the unprocessed RNA-seq data is available online in the Gene Expression Omnibus database (https://www.ncbi.nlm.nih.gov) under accession number GSE145369.

Acknowledgements

This work is funded by the Deutsche Forschungsgemeinschaft (DFG, German Research Foundation) SFB1454 (project number 432325352) and under Germany´s Excellence Strategy EXC2151 (project number 390873048) (to S.B.), a European Federation for the Study of Diabetes (EFSD)/Lilly Research Grant Fellowship from the European Federation for the Study of Diabetes (to B.G.), Dutch Research Council (NWO) Graduate School Program 022.006.010 (to H.J.P.v.d.Z.), and the Dutch Organization for Scientific Research (ZonMW TOP Grant 91214131 to B.G. and M.Y.). We thank Frank Otto and Arifa Ozir-Fazalalikhan for their invaluable technical help. The authors declare no competing interests.

References

1. Brestoff JR, Artis D. Immune regulation of metabolic homeostasis in health and disease. Cell. 2015;161(1):146-60.
2. Hotamisligil GS. Inflammation, metaflammation and immunometabolic disorders. Nature. 2017;542(7640):177-85.
3. Lackey DE, Olefsky JM. Regulation of metabolism by the innate immune system. Nat Rev Endocrinol. 2016;12(1):15-28.
4. Hotamisligil GS, Murray DL, Choy LN, Spiegelman BM. Tumor necrosis factor alpha inhibits signaling from the insulin receptor. Proc Natl Acad Sci U S A. 1994;91(11):4854-8.
5. Shulman GI. Ectopic fat in insulin resistance, dyslipidemia, and cardiometabolic disease. N Engl J Med. 2014;371(23):2237-8.
6. Neuschwander-Tetri BA. Hepatic lipotoxicity and the pathogenesis of nonalcoholic steatohepatitis: the central role of nontriglyceride fatty acid metabolites. Hepatology. 2010;52(2):774-88.
7. Lanthier N, Molendi-Coste O, Horsmans Y, van Rooijen N, Cani PD, Leclercq IA. Kupffer cell activation is a causal factor for hepatic insulin resistance. Am J Physiol Gastrointest Liver Physiol. 2010;298(1):G107-16.
8. Morinaga H, Mayoral R, Heinrichsdorff J, Osborn O, Franck N, Hah N, et al. Characterization of distinct subpopulations of hepatic macrophages in HFD/obese mice. Diabetes. 2015;64(4):1120-30.
9. Martinez-Pomares L. The mannose receptor. J Leukoc Biol. 2012;92(6):1177-86.
10. Takahashi K, Donovan MJ, Rogers RA, Ezekowitz RA. Distribution of murine mannose receptor expression from early embryogenesis through to adulthood. Cell Tissue Res. 1998;292(2):311-23.
11. Burgdorf S, Kautz A, Bohnert V, Knolle PA, Kurts C. Distinct pathways of antigen uptake and intracellular routing in CD4 and CD8 T cell activation. Science. 2007;316(5824):612-6.
12. Burgdorf S, Lukacs-Kornek V, Kurts C. The mannose receptor mediates uptake of soluble but not of cell-associated antigen for cross-presentation. J Immunol. 2006;176(11):6770-6.
13. Jordens R, Thompson A, Amons R, Koning F. Human dendritic cells shed a functional, soluble form of the mannose receptor. Int Immunol. 1999;11(11):1775-80.
14. Martinez-Pomares L, Mahoney JA, Kaposzta R, Linehan SA, Stahl PD, Gordon S. A functional soluble form of the murine mannose receptor is produced by macrophages in vitro and is present in mouse serum. J Biol Chem. 1998;273(36):23376-80.
15. Saha B, Tornai D, Kodys K, Adejumo A, Lowe P, McClain C, et al. Biomarkers of Macrophage Activation and Immune Danger Signals Predict Clinical Outcomes in Alcoholic Hepatitis. Hepatology. 2019;70(4):1134-49.
16. Suzuki Y, Shirai M, Asada K, Yasui H, Karayama M, Hozumi H, et al. Macrophage mannose receptor, CD206, predict prognosis in patients with pulmonary tuberculosis. Sci Rep. 2018;8(1):13129.

17. Rodgaard-Hansen S, Rafique A, Weis N, Wejse C, Nielsen H, Pedersen SS, et al. Increased concentrations of the soluble mannose receptor in serum from patients with pneumococcal bacteraemia, and prediction of survival. Infect Dis (Lond). 2015;47(4):203-8.

18. Ding D, Song Y, Yao Y, Zhang S. Preoperative serum macrophage activated biomarkers soluble mannose receptor (sMR) and soluble haemoglobin scavenger receptor (sCD163), as novel markers for the diagnosis and prognosis of gastric cancer. Oncol Lett. 2017;14(3):2982-90.

19. Loonen AJM, Leijtens S, Serin O, Hilbink M, Wever PC, van den Brule AJC, et al. Soluble mannose receptor levels in blood correlate to disease severity in patients with community-acquired pneumonia. Immunol Lett. 2019;206:28-32.

20. Andersen ES, Rodgaard-Hansen S, Moessner B, Christensen PB, Moller HJ, Weis N. Macrophage-related serum biomarkers soluble CD163 (sCD163) and soluble mannose receptor (sMR) to differentiate mild liver fibrosis from cirrhosis in patients with chronic hepatitis C: a pilot study. Eur J Clin Microbiol Infect Dis. 2014;33(1):117-22.

21. Schuette V, Embgenbroich M, Ulas T, Welz M, Schulte-Schrepping J, Draffehn AM, et al. Mannose receptor induces T-cell tolerance via inhibition of CD45 and up-regulation of CTLA-4. Proc Natl Acad Sci U S A. 2016;113(38):10649-54.

22. Van den Bossche J, O'Neill LA, Menon D. Macrophage Immunometabolism: Where Are We (Going)? Trends Immunol. 2017;38(6):395-406.

23. Viola A, Munari F, Sanchez-Rodriguez R, Scolaro T, Castegna A. The Metabolic Signature of Macrophage Responses. Front Immunol. 2019;10:1462.

24. Xue J, Schmidt SV, Sander J, Draffehn A, Krebs W, Quester I, et al. Transcriptome-based network analysis reveals a spectrum model of human macrophage activation. Immunity. 2014;40(2):274-88.

25. Martinez-Pomares L, Crocker PR, Da Silva R, Holmes N, Colominas C, Rudd P, et al. Cell-specific glycoforms of sialoadhesin and CD45 are counter-receptors for the cysteine-rich domain of the mannose receptor. J Biol Chem. 1999;274(49):35211-8.

26. Pilling D, Fan T, Huang D, Kaul B, Gomer RH. Identification of markers that distinguish monocyte-derived fibrocytes from monocytes, macrophages, and fibroblasts. PLoS One. 2009;4(10):e7475.

27. Shrivastava P, Katagiri T, Ogimoto M, Mizuno K, Yakura H. Dynamic regulation of Src-family kinases by CD45 in B cells. Blood. 2004;103(4):1425-32.

28. Chen J. The Src/PI3K/Akt signal pathway may play a key role in decreased drug efficacy in obesity-associated cancer. J Cell Biochem. 2010;110(2):279-80.

29. Bai D, Ueno L, Vogt PK. Akt-mediated regulation of NFkappaB and the essentialness of NFkappaB for the oncogenicity of PI3K and Akt. Int J Cancer. 2009;125(12):2863-70.

30. Xie X, Lan T, Chang X, Huang K, Huang J, Wang S, et al. Connexin43 mediates NF-kappaB signalling activation induced by high glucose in GMCs: involvement of c-Src. Cell Commun Signal. 2013;11(1):38.

31. Abu-Amer Y, Ross FP, McHugh KP, Livolsi A, Peyron JF, Teitelbaum SL. Tumor necrosis factor-alpha activation of nuclear transcription factor-kappaB in marrow macrophages is mediated by c-Src tyrosine phosphorylation of Ikappa Balpha. J Biol Chem. 1998;273(45):29417-23.

32. Cheng J, Phong B, Wilson DC, Hirsch R, Kane LP. Akt fine-tunes NF-kappaB-dependent gene expression during T cell activation. J Biol Chem. 2011;286(41):36076-85.

33. Lumeng CN, Bodzin JL, Saltiel AR. Obesity induces a phenotypic switch in adipose tissue macrophage polarization. J Clin Invest. 2007;117(1):175-84.

34. Rauen J, Kreer C, Paillard A, van Duikeren S, Benckhuijsen WE, Camps MG, et al. Enhanced cross-presentation and improved CD8+ T cell responses after mannosylation of synthetic long peptides in mice. PLoS One. 2014;9(8):e103755.

35. Kreer C, Kuepper JM, Zehner M, Quast T, Kolanus W, Schumak B, et al. N-glycosylation converts non-glycoproteins into mannose receptor ligands and reveals antigen-specific T cell responses in vivo. Oncotarget. 2017;8(4):6857-72.

36. Jaitin DA, Adlung L, Thaiss CA, Weiner A, Li B, Descamps H, et al. Lipid-Associated Macrophages Control Metabolic Homeostasis in a Trem2-Dependent Manner. Cell. 2019;178(3):686-98 e14.

37. Klotz L, Hucke S, Thimm D, Classen S, Gaarz A, Schultze J, et al. Increased antigen cross-presentation but impaired cross-priming after activation of peroxisome proliferator-activated receptor gamma is mediated by up-regulation of B7H1. J Immunol. 2009;183(1):129-36.

38. Lluis JM, Buricchi F, Chiarugi P, Morales A, Fernandez-Checa JC. Dual role of mitochondrial reactive oxygen species in hypoxia signaling: activation of nuclear factor-{kappa}B via c-SRC and oxidant-dependent cell death. Cancer Res. 2007;67(15):7368-77.

39. Westcott DJ, Delproposto JB, Geletka LM, Wang T, Singer K, Saltiel AR, et al. MGL1 promotes adipose tissue inflammation and insulin resistance by regulating 7/4hi monocytes in obesity. J Exp Med. 2009;206(13):3143-56.

40. van Vliet SJ, Gringhuis SI, Geijtenbeek TB, van Kooyk Y. Regulation of effector T cells by antigen-presenting cells via interaction of the C-type lectin MGL with CD45. Nat Immunol. 2006;7(11):1200-8.

Supplementary Materials and Methods

Antibodies and Reagents

α-mouse actin (20-33), α-phosphotyrosine (4G10) and α-mouse GAPDH (10B13) were obtained from Merck, α-mouse vinculin (4650), α-mouse IκBa (44D4), α-mouse PCNA (PC10), α-mouse Akt (9272), α-mouse pAkt (Ser473)(9271), α-mouse Src (L4A1), α-mouse pSrc (Tyr416)(2101) and α-mouse p65 (D14E12) from Cell Signaling Technology, α-mouse calnexin (ab22595) from Abcam and α-mouse p50 (E10) from Santa Cruz. All antibodies used in flow cytometry are listed in Supplementary Table 1. Recombinant MR was obtained from R&D Systems, KX2-391 from Biotrend, A-419259 from Biomol, MK-2206 from Enzo Life Sciences, Biotin from Roth, SF1670 from Merck and rhM-CSF from BioLegend. All other chemicals were obtained from Sigma.

Purification of sMR from the supernatant of MR-expressing cells

Supernatant of bone marrow-derived macrophages was collected and loaded on an affinity chromatography column containing Sepharose beads that were covalently linked to an anti-MR antibody (MR5D3, BIO-RAD). After extensive washing, sMR was eluted in 0.1 M Glycin (pH 2.5), neutralized with 1 M Tris (pH 9.0) and dialyzed against PBS containing 10% PEG for 24 h.

Sample preparation for Western Blot analysis

For whole cell lysates, samples were lysed in 10 mM triethanolamine, 150 mM NaCl, 1 mM $MgCl_2$, 1 mM $CaCl_2$ and 1% Triton X-100. For the extraction of nuclear extracts, cells were lysed first in 50 mM HEPES-KOH, 1 mM EDTA (pH 8.0), 140 mM NaCl, 0.25% Triton X-100, 0.5% Igepal and 10% glycerol and the cytosolic fraction was harvested. Afterwards, pellets were resuspended in 10 mM Tris-HCl (pH 8.0), 1 mM EDTA, 100 mM NaCl, 0.5 mM EGTA, 0.1% Sodium desoxycholic acid and 0.5% sodium N-lauryl sarcosine, sonicated and centrifuged, yielding the nuclear fraction.

Surface biotinylation and co-immunoprecipitation experiments

Bone marrow-derived macrophages were incubated with 0.5 mg/ml biotin for 30 min and washed extensively. Afterwards, cells were lysed and 10 μg/ml FcMR was added for 1 h on ice. Subsequently, FcMR was immunoprecipitated using protein A/G-based affinity chromatography and samples were loaded on an SDS-PAGE for analysis by Western Blot using streptavidin or a CD45-specific antibody. Alternatively, a CD45-specific antibody was

added to macrophage lysates and precipitated by protein A/G-based affinity chromatography for subsequent far Western Blot analysis using FcMR.

CD45 phosphatase assay

CD45 was immunoprecipitated from macrophage lysates and incubated with 2 mM pNPP for 18 h at 37°C in the presence or absence of 1 μM of the CD45-specific inhibitor SF1670. Dephosphorylation of pNPP was quantified by colorimetry at 405 nm. Alternatively, immunoprecipitated CD45 was incubated with 0.25 μg of the biotinylated peptide TATEGQpYQPQ for 18 h at 37 °C in the presence or absence of SF1670. Phosphorylated TATEGQpYQPQ was monitored after affinity chromatography using streptavidin-agarose, staining with the phosphospecific primary antibody 4G10 (Milipore), a HRP-conjugated secondary antibody and addition of the HRP substrate TMB One (Kementec).

siRNA-mediated down-regulation of CD45

siRNA against CD45 (Mm-Ptprc_6 Flexitube siRNA, Qiagen) or control siRNA (AAAAACAUGCAGAAAUGCUGU; containing a specific sequence of the luciferase gene) were obtained from Qiagen. After five days of culture in GM-CSF-containing medium, cells were electroporated with 4 μg siRNA using a Gene Pulser Xcell Electroporation Systems (Bio-Rad) with two sequential pulses of 1000 V for 0.5 ms each. Cells were incubated for 2 days before subsequent experiments were performed.

Blood monocyte-derived macrophages and siRNA-mediated down-regulation of MR expression

Human $CD14^+$ monocytes were isolated from blood of anonymous healthy volunteers, as described previously (1), and cultured in RPMI 1640 (Invitrogen) supplemented with 10% heat-inactivated FSC, 100 U/ml penicillin, 100 μg/ml streptomycin and 50 ng/mL of recombinant human M-CSF (BioLegend) in plates with Nunclon™ Delta Surface coating (Nunc). On day 4 of differentiation, cells were electroporated with either 455 nM anti-*Mrc1* siRNA or 455 nM scrambled siRNA (Dharmacon) using the Neon® transfection system (Invitrogen) using one pulse of 1600V for 20 ms. Cells were incubated for 2 days and next incubated for 24 h with 100 ng/ml LPS and 50 ng/ml IFN-γ. Supernatant was harvested after 24 h for analyses of TNF, IL-6, and IL-1β by ELISA using a commercially available kit (BioLegend).

RNA isolation and RNAseq analysis

RNA of $5x10^6$ bone marrow-derived macrophages treated with FcMR or isotype control for 4, 12, and 24 h was isolated with Trizol and miRNeasy micro kit (Qiagen) according to the manufacturer's protocol. RNA quality was assessed by visualization of 28S and 18S band integrity on a Tapestation 2200 (Agilent). 100 ng of RNA was converted into cDNA libraries using the TruSeq RNA library preparation kit v2. Size distribution of cDNA libraries was measured using the Agilent high sensitivity DNA assay on a Tapestation 2200 (Agilent). cDNA libraries were quantified using KAPA Library Quantification Kits (Kapa Biosystems). After cluster generation on a cBot, 75 bp single read sequencing was performed on a HiSeq1500.

Bioinformatic analysis

After base calling and de-multiplexing using CASAVA version 1.8.2 and subsequent quality control using fastQC, the 75 bp single-end reads were pseudoaligned to the mm10-based mouse Gencode reference transcriptome vM16 using kallisto version 0.44.0. Transcript abundance estimations were imported to R and summarized on gene level using tximport (2). Downstream analyses were performed using DESeq2 (3). After filtering of lowly expressed genes (rowSums > 10) and variance stabilizing transformation, principal component analysis was performed on all present genes using the prcomp package. Differential expression analysis was performed comparing FcMR-treated samples versus controls for each time point without pre-defined $\log_2$ fold change threshold and using independent hypothesis weighting (IHW) as the multiple testing procedure. Genes with an adjusted p-value < 0.05 and a fold change (FC) > 2 were determined as significantly differentially expressed. Normalized and z-scaled expression values of the union of differentially expressed (DE) genes over all three time points were visualized in a heatmap. Gene ontology enrichment analyses were performed on those genes shared between all three DE gene sets (shared), as well as the respective gene sets for each time point (4 h, 12 h, and 24 h) and those genes unique for each time point (4h.u, 12 h.u, and 24 h.u) using the R package ClusterProfiler and visualized in a dot plot. Based on the differential expression analysis, genes with significant upregulation in at least two consecutive time points were selected and ranked according to their FC at each timepoint. Normalized and z-scaled expression values of the union of the top 25 genes for each comparison were visualized in a heatmap. Furthermore, enrichment analysis on the FcMR-specific DE genes for each time point was performed based on 49 previously defined, stimulus-specific macrophage expression signatures encompassing 28 different immunological stimuli, using ClusterProfiler's 'enricher' function. Significantly enriched

signatures were visualized in a dot plot and normalized and z-scaled expression values of the genes to the enriched signatures were plotted in a heatmap. To identify transcriptional regulators responsible for the FcMR-induced changes in gene expression, transcription factor motif enrichment analyses was performed using ClusterProfiler's 'enricher' function based on the MSigDB motif gene sets on the FcMR-specific DE genes for each time point. Motifs with q-value < 0.1 were selected and results were visualized in networks showing the enriched TF motifs and their potential targets among the DE genes of the respective comparison using Cytoscape v3.4.0. For determination of the *Cd45* transcript variant expressed in the cells of this data set, reads were aligned to the reference genome mm10 using Hisat2 v2.1.0 (4) and visualized using the R package Gviz (5). For additional analysis of the NF-κB pathway, we downloaded a comprehensive list of NF-κB target genes from *https://www.bu.edu/nf-kb/gene-resources/target-genes/* and matched the human genes with their murine orthologs. The curated NF-κB target gene list can be found as Dataset S1. Intersecting the resulting list of 417 murine NF-κB target genes with the set of genes detected in our bulk RNA-seq experiment revealed the presence of 351 genes in our data set, of which 118 genes were significantly DE on at least one time point comparing the FcMR-treated cells with controls. Normalized and z-scaled expression values of the 351 present NF-κB target genes were visualized in a heatmap. In addition, fold changes and mean expression values of the significantly DE genes comparing the FcMR-treated cells with controls at the respective time points were visualized in MA plots with colored dots indicating NF-κB targets among the sets of DE genes.

ChIP-qPCR

Bone marrow-derived macrophages were stimulated with 10 μg/ml FcMR or isotype control for 1 h prior to stimulation with 200 ng/ml LPS for another 90 min. Cell fixation, chromatin isolation and ChIP was performed as described previously (6). Briefly, cells were fixed in 1% methanol-free formaldehyde for 5 min at RT, followed by blocking in 125 mM glycine. Nuclei were isolated by NEXSON and chromatin preparation was done using a Covaris S220 focused ultrasonicator (Peak Power: 75 W; Duty factor: 2%; Cycles/burst: 200; 8 min and Peak Power: 140 W; Duty factor: 5%; Cycles/burst: 200; 20 min, respectively). Chromatin preparation was incubated overnight at 4 °C with anti-p65 (clone D14E12, Cell Signaling) or isotype control (rabbit IgG, 31235, Thermo Scientific), followed by incubation for 2 h with Dynabeads (10003D, Thermo Scientific). Samples were eluted by 50 mM glycine pH 2.8 and decrosslinked with Proteinase K and RNase A for 30 min at 37°C and overnight at 65°C. DNA was purified by NucleoSpin Gel and PCR Clean-up Kit (740609.250, Macherey-

Nagel). qPCR was performed with Absolute qPCR Mix (AB1162B, Thermo Scientific) on a CFX96 Real-Time System (BioRad) using 5'-GAGGCTCCGTGGAAAACTCACTTG-3' and 5'-GCAGAGCAGCTTGAGAGTTGGGAA-3' (TNF promoter region 1) and 5'-CAGTTCTCAGGGTCCTATACAACACA-3' and 5'-GGTAGTGGCCCTACACCTCT GTC-3' (TNF promoter region 2) as primers.

Human samples

Serum samples from twenty-six healthy, weight-stable, nonsmoking Caucasian volunteer subjects, 12 lean (2 males, 10 females, BMI 23.3 +/- 0.5 kg/m^2) and 14 obese (2 males, 12 females, BMI 35.2 +/- 1.2 kg/m^2), this latter before and after weight loss, were collected in the framework of a clinical trial (7) and used to measure circulating sMR in a subset of still available samples. This study (Clinical Trial Registration No. NTR2401) was approved by the Medical Ethics Committee of the Leiden University Medical Centre and performed in accordance with the principles of the revised Declaration of Helsinki. All volunteers gave written informed consent before participation.

Plasma analysis

Blood samples were collected from the tail tip of 4 h-fasted mice using chilled paraoxon-coated capillaries. sMR serum levels were determined after immune precipitation using a MR-specific antibody, followed by fluorimetry. Blood glucose levels were determined using a Glucometer (Accu-Check, Roche Diagnostics). Plasma total cholesterol (TC; Instruchemie), triglycerides (TG; Instruchemie) and insulin (Chrystal Chem) were determined using commercially available kits according to the manufacturer's instructions. The homeostatic model assessment of insulin resistance (HOMA-IR) adapted to mice was calculated as ([glucose (mg/dl)*0.055] × [insulin (ng/ml) × 172.1])/3857 and used as a surrogate measure of whole-body insulin resistance (8). Plasma alanine aminotransferase (ALAT) was measured using a Reflotron® kit (Roche diagnostics).

Body composition and indirect calorimetry

Body composition was measured by MRI using an EchoMRI (Echo Medical Systems). Groups of 6-8 mice with free access to food and water were subjected to individual indirect calorimetric measurements at 16 weeks after the start of diet feeding for a period of 5 consecutive days using a Comprehensive Laboratory Animal Monitoring System (Columbus Instruments). Before the start of the measurements, the animals were acclimated to the cages and the single housing for a period of 48 h. Feeding behavior was assessed by real-time

food intake. Spontaneous locomotor activity was determined by the measurement of beam breaks. Oxygen consumption and carbon dioxide production were measured at 15 min intervals. Energy expenditure and carbohydrate and fatty acid oxidation were calculated and normalized for body surface area ($kg^{0.75}$), as previously described (9). The adipocyte number per fat pad and mean adipocyte volume were determined as previously described (10).

Insulin and glucose tolerance tests

Whole-body insulin sensitivity was assessed after the indicated time on CD or HFD in 4 h fasted mice by an i.p. insulin tolerance test (ipITT). After an initial blood collection (t=0), an i.p. bolus of insulin (1 U/kg lean body mass; NOVORAPID, Novo Nordisk) was administered to the mice. Blood glucose was measured by tail bleeding at indicated time points after insulin administration using a Glucometer. Whole-body glucose tolerance was assessed after the indicated time on CD or HFD in 6 h fasted mice by an intraperitoneal glucose tolerance test (ipGTT). After an initial blood collection (t=0), an i.p. injection of glucose (2g D-Glucose/kg total body weight, Sigma-Aldrich) was administered in conscious mice. Blood glucose was measured by tail bleeding at indicated time points after glucose administration using a Glucometer (Accu-Check, Roche Diagnostics). At 15 minutes, blood was also collected for analysis of plasma insulin levels as described above.

Histological analyses

A piece of eWAT or liver (~30 mg) was fixed in 4% paraformaldehyde (PFA; Sigma-Aldrich), paraffin-embedded, sectioned at 4 μm and stained with Hematoxylin and Eosin (H&E). Six fields at 20x magnification (total area 1.68 mm^2) were used for the analysis of crown-like structures and hepatic steatosis.

Hepatic lipid composition

Liver lipids were extracted as previously described (11). Briefly, liver samples (~50 mg) were homogenized in ice-cold methanol. After centrifugation, lipids were extracted with CH_3OH:$CHCl_3$ (1:3 v/v), followed by phase separation with centrifugation (13,000 x g; 15 min at RT). The organic phase was dried and dissolved in 2% Triton X-100 in water. Triglycerides (TG), total cholesterol (TC) and phospholipids (PL) concentrations were measured using commercial kits (Roche Molecular Biochemicals). Liver lipids were expressed as nanomoles per mg protein, which was determined using the Bradford protein assay kit (Sigma-Aldrich).

RNA purification and qRT-PCR

RNA was extracted from snap-frozen tissue samples using Tripure RNA Isolation reagent (Roche Diagnostics). Total RNA (1 μg) was reverse transcribed and quantitative real-time PCR was next performed with the SYBR Green Core Kit on a MyIQ thermal cycler (Bio-Rad). mRNA expression was normalized to *Rplp0* mRNA content and expressed as fold change compared to wild-type CD-fed mice using the ΔΔCT method. Primers are listed in Supplementary Table 2.

Isolation of stromal vascular fraction from adipose tissue

Epididymal adipose tissues were collected in PBS, then minced and digested for 1 h at 37°C in HEPES-buffered Krebs solution (pH 7.4) containing 0.5 mg/mL collagenase type I from *Clostridium histolyticum* (Sigma-Aldrich), 2% (w/v) bovine serum albumin (BSA, fraction V, Sigma-Aldrich) and 6 mM glucose, as previously described (12). Disaggregated adipose tissues were passed through 100 μm cell strainers or 200 μm filters and washed with PBS supplemented with 2.5 mM EDTA and 5% FCS. Filtrate was either directly centrifuged (350 x *g*, 10 min at RT) or rested for 10 minutes, after which infranatant was collected and centrifuged. After centrifugation, the supernatant was discarded and the pellet containing the stromal vascular fraction (SVF) was treated with erythrocyte lysis buffer (BD Biosciences). After washing, cells were either directly counted, or macrophages were isolated using LS columns and F4/80 microbeads according to the manufacturer's protocol. Cells were next stained with the live/dead marker Aqua or Zombie-UV (Invitrogen), fixed with 1.9% paraformaldehyde (Sigma-Aldrich) and stored in FACS buffer (PBS, 2 mM EDTA, 0.5% BSA [w/v]) at 4°C in the dark until subsequent analysis performed within 4 days.

Isolation of leukocytes from liver tissue

Livers were collected in ice-cold RPMI 1640 + Glutamax (Life Technologies), minced and digested for 45 min at 37°C in RPMI 1640 + Glutamax supplemented with 1 mg/mL collagenase type IV from *Clostridium histolyticum*, 2000 U/mL DNase (both Sigma-Aldrich) and 1 mM $CaCl_2$, as previously described (12). In short, the digested tissues were next passed through 100 μm cell strainers and washed with PBS/EDTA/FCS. Following centrifugation (530 x g, 10 min at 4 °C), the cell pellet was resuspended in PBS/EDTA/FCS and centrifuged at 50 x g to pellet hepatocytes (3 minutes at 4 °C). The supernatant was next collected and pelleted (530 x g, 10 min at 4 °C), followed by treatment with erythrocyte lysis buffer. After washing, either macrophages or total leukocytes were isolated using LS columns and F4/80 or CD45 MicroBeads (35 μl beads per liver; Miltenyi Biotec),

respectively, according to the manufacturer's protocol. Isolated $CD45^+$ cells were counted and processed for flow cytometry as for SVF, and $F4/80^+$ cells were stimulated with FcMR and LPS as described above.

Isolation of peritoneal macrophages

Peritoneal wash was collected in PBS supplemented with 2 mM EDTA and centrifuged (530 x g, 10 min at 4°C). Cell pellet was treated with erythrocyte lysis buffer, counted and processed for flow cytometry as for SVF, or macrophages were isolated using MS columns and F4/80 microbeads according to the manufacturer's protocol.

Isolation of splenic macrophages

Spleens were collected in ice-cold RPMI 1640 + Glutamax, minced and digested for 20 min at 37°C in RPMI 1640 + Glutamax supplemented with 1 mg/mL collagenase D (Sigma) and 2000 U/mL DNase. The digested tissues were next passed through 100 µm cell strainers and washed with PBS/EDTA/FCS. Following centrifugation (530 x g, 10 min at 4°C), the cell pellet was treated with erythrocyte lysis buffer. Cells were either counted and processed for flow cytometry as for SVF, or macrophages were isolated using MS columns and F4/80 microbeads according to the manufacturer's protocol.

Flow cytometry

For analysis of myeloid subsets, part of the cells was first permeabilized with 0.5% saponin (Sigma-Aldrich) or eBioscience permeabilization buffer (Invitrogen) and stained with an antibody against YM1 conjugated to biotin prior to staining with an antibody cocktail including streptavidin-PerCP. Cells were either next or directly stained with antibodies directed against CD11b, CD11c, CD45, CD45.2, CD45RA, CD45RB, CD45RC, CD64, F4/80, Ly6C, and Siglec-F in either 0.5% saponin, permeabilization, or FACS buffer. For assessing MR-expressing cells in obesity, samples were additionally incubated with antibodies specific for CD31, CD146, and MR. For analysis of lymphocyte subsets, cells were stained with antibodies directed against B220, CD3e, CD11b, CD11c, GR-1, NK1.1 (all for lineage cocktail), CD4, CD8a, CD19, IL-13, and Thy1.2. For detection of intracellular cytokines, isolated immune cells were first *ex vivo* cultured for 4 hours in culture medium in the presence of 100 ng/mL phorbol myristate acetate (PMA), 1 µg/ml ionomycin and 10 µg/ml Brefeldin A (all from Sigma-Aldrich) prior to viability staining and fixation. Cells were measured on a FACSCanto flow cytometer or LSR-II (both BD Biosciences), and gates were set according to Fluorescence Minus One (FMO) controls. Gating strategies can be

found in Supplementary Figure 9. The source and information on antibodies used for flow cytometry are listed in Supplementary Table 1.

Extracellular flux analysis

Extracellular Flux Analysis was performed as described before (13). Briefly, BMDMs or human moM's were incubated with FcMR or isotype control (18h) or rhMR (5h) respectively and settled in RPMI-1640 (Sigma; pH = 7.4) supplemented with 5% FCS on a 96-well assay plate (Agilent) and rested at 37°C in 0% CO_2 for 1 hour. Extracellular acidification rate (ECAR) was recorded with the XF96e Extracellular Flux analyzer (Agilent) in response to glucose (10 mM; Sigma) and oligomycin (1.5 μM; Cayman Chemical) injection.

Supplementary references

1. Hussaarts L, Smits HH, Schramm G, van der Ham AJ, van der Zon GC, Haas H, et al. Rapamycin and omega-1: mTOR-dependent and -independent Th2 skewing by human dendritic cells. Immunol Cell Biol. 2013;91(7):486-9.
2. Soneson C, Love MI, Robinson MD. Differential analyses for RNA-seq: transcript-level estimates improve gene-level inferences. F1000Res. 2015;4:1521.
3. Love MI, Huber W, Anders S. Moderated estimation of fold change and dispersion for RNA-seq data with DESeq2. Genome Biol. 2014;15(12):550.
4. Kim D, Paggi JM, Park C, Bennett C, Salzberg SL. Graph-based genome alignment and genotyping with HISAT2 and HISAT-genotype. Nat Biotechnol. 2019;37(8):907-15.
5. Hahne F, Ivanek R. Visualizing Genomic Data Using Gviz and Bioconductor. Methods Mol Biol. 2016;1418:335-51.
6. Arrigoni L, Richter AS, Betancourt E, Bruder K, Diehl S, Manke T, et al. Standardizing chromatin research: a simple and universal method for ChIP-seq. Nucleic Acids Res. 2016;44(7):e67.
7. Wijngaarden MA, van der Zon GC, van Dijk KW, Pijl H, Guigas B. Effects of prolonged fasting on AMPK signaling, gene expression, and mitochondrial respiratory chain content in skeletal muscle from lean and obese individuals. Am J Physiol Endocrinol Metab. 2013;304(9):E1012-21.
8. Lee S, Muniyappa R, Yan X, Chen H, Yue LQ, Hong EG, et al. Comparison between surrogate indexes of insulin sensitivity and resistance and hyperinsulinemic euglycemic clamp estimates in mice. Am J Physiol Endocrinol Metab. 2008;294(2):E261-70.
9. Hussaarts L, Garcia-Tardon N, van Beek L, Heemskerk MM, Haeberlein S, van der Zon GC, et al. Chronic helminth infection and helminth-derived egg antigens promote adipose tissue M2 macrophages and improve insulin sensitivity in obese mice. FASEB J. 2015;29(7):3027-39.
10. van Beek L, Vroegrijk IO, Katiraei S, Heemskerk MM, van Dam AD, Kooijman S, et al. FcRgamma-chain deficiency reduces the development of diet-induced obesity. Obesity (Silver Spring). 2015;23(12):2435-44.
11. Geerling JJ, Boon MR, van der Zon GC, van den Berg SA, van den Hoek AM, Lombes M, et al. Metformin lowers plasma triglycerides by promoting VLDL-triglyceride clearance by brown adipose tissue in mice. Diabetes. 2014;63(3):880-91.
12. van der Zande HJP, Gonzalez MA, de Ruiter K, Wilbers RHP, Garcia-Tardon N, van Huizen M, et al. The helminth glycoprotein omega-1 improves metabolic homeostasis in obese mice through type 2 immunity-independent inhibition of food intake. FASEB J. 2021;35(2):e21331.
13. Pelgrom LR, van der Ham AJ, Everts B. Analysis of TLR-Induced Metabolic Changes in Dendritic Cells Using the Seahorse XF(e)96 Extracellular Flux Analyzer. Methods Mol Biol. 2016;1390:273-85.

Supplementary information

Supplementary Table 1. FACS antibodies.

Target	Clone	Conjugate	Source	Identifier
B220	RA3-6B2	FITC	eBioscience	11-0452
B220	RA3-6B2	eF450	eBioscience	48-0452
CD3e	17A2	APC	eBioscience	17-0032
CD3e	17A2	FITC	eBioscience	11-0032
CD4	GK1.5	PE-Cy7	eBioscience	25-0041
CD4	GK1.5	PerCP-eF710	eBioscience	46-0041
CD8a	53-6.7	APC-Cy7	Biolegend	100714
CD11b	M1/70	FITC	eBioscience	11-0112
CD11b	M1/70	PE-Cy7	eBioscience	25-0112
CD11c	HL3	FITC	BD Biosciences	553801
CD11c	HL3	V450	BD Biosciences	560521
CD19	eBio1D3	eF450	eBioscience	48-0193
CD31	MEC 13.3	FITC	BD Biosciences	561813
CD45	30-F11	BV785	Biolegend	103149
CD45.2	104	FITC	Biolegend	109806
CD45RA	RA3-6B2	Pacific Blue	Biolegend	103230
CD45RB	16A	FITC	BD Biosciences	553099
CD45RC	DNL-1.9	PE	BD Biosciences	557357
CD64	X54-5/7.1	PE	Biolegend	139304
CD146	ME-9F1	PE-Cy7	Biolegend	134713
CD206/MR	MR5D3	APC	Bio-Rad	MCA2235
F4/80	BM8	APC	eBioscience	17-4801
F4/80	BM8	BV711	Biolegend	123147
GR-1	RB6-8C5	FITC	BD Biosciences	553126
IL-13	eBio13A	eF450	eBioscience	48-7133
Ly6C	HK1.4	APC-Cy7	Biolegend	128025
NK1.1	PK136	FITC	eBioscience	11-5941
Siglec-F	E50-2440	BV605	BD Biosciences	740388
Siglec-F	E50-2440	PE	BD Biosciences	552126
Thy1.2	30-H12	APC-eF780	eBioscience	47-0902
YM1	Polyclonal	Biotin	R&D Systems	BAF2446
Other reagents			**Source**	**Identifier**
LIVE/DEAD™ Fixable Aqua Dead Cell Stain Kit			Invitrogen	L34957
Zombie UV™ Fixable Viability Kit			Biolegend	423107
Streptavidin - PerCP			BD Biosciences	554064

Supplementary Table 2. qPCR primers.

Gene	Accession number	Forward primer	Reverse primer
Acaca	NM_133360.2	CAGCTGGTGCAGAGGTACCG	TCTACTCCGCAGGTACTGCCG
Acadm	NM_007382	TACCCGTTCCCTCTCATCAA	CACCCATACGCCAACTCTTC
Acox1	NM_015729	GGGACCCACAAGCCTCTGCCA	GTGCCGTCAGGCTTCACCTGG
Adipoq	NM_009605	GGAATGACAGGAGCTGAAGG	CGAATGGGTACATTGGGAAC
Ccl2	NM_011333.3	TCAGCCAGATGCAGTTAACGCCC	GCTTCTTTGGGACACCTGCTGCT
Cd36	NM_001159558	GCAAAGAACAGCAGCAAAATC	CAGTGAAGGCTCAAAGATGG
Cebpa	NM_007678.3	TGCCGGGAGAACTCTAACTC	CTCTGGAGGTGACTGCTCAT
Cidea	NM_007702	CTCGGCTGTCTCAATGTCAA	CCGCATAGACCAGGAACTGT
Cidec	NM_178373	CCATCAGAACAGCGCAAGAAG	AGAGGGTTGCCTTCACGTTC
Cox8b	NM_007751.3	GACCCCGAGAATCATGCCAA	CCTGCTCCACGGCGGAA
Cpt1a	NM_013495	AGGAGACAAGAACCCCAACA	AAGGAATGCAGGTCCACATC
Dlk1	NM_010052.5	GTACCCCTAACCCATGCGAG	TGCACAGACACTCGAAGCTC
Fabp1	NM_017399.4	GCCACCATGAACTTCTCCGGCA	GGTCCTCGGGCAGACCTATTGC
Fasn	NM_007988	CACAGGCATCAATGTCAACC	TTTGGGAAGTCCTCAGCAAC
Infg	NM_008337	CGGCACAGTCATTGAAAGCC	TGTCACCATCCTTTTGCCAGT
Il1b	NM_008361	GACCCCAAAAGATGAAGGGCT	ATGTGCTGCTGCGAGATTTG
Il4	NM_021283	CCTCACAGCAACGAAGAACA	ATCGAAAAGCCCGAAAGAGT
Il6	NM_031168.1	TGTGCAATGGCAATTCTGAT	CTCTGAAGGACTCTGGCTTTG
Il10	NM_010548	GACAACATACTGCTAACCGACTC	ATCACTCTTCACCTGCTCCACT
Il12a	NM_001159424	GGTGAAGACGGCCAGAGAAA	GTAGCCAGGCAACTCTCGTT
Il17a	NM_010552	TCATCCCTCAAAGCTCAGCG	TTCATTGCGGTGGAGAGTCC
Itgax	NM_021334.2	GCCACCAACCCTTCCTGGCTG	TTGGACACTCCTGCTGTGCAGTTG
Lep	NM_008493	CCCTGTGTCGGTTCCTGTGGC	GCGGATACCGACTGCGTGTGT
Mrc1	NM_008625.2	TTCAGCTATTGGACGCGAGG	GAATCTGACACCCAGCGGAA
Pparg	NM_011146	TACATAAAGTCCTTCCCGCTGAC	GTGATTTGTCCGTTGTCTTTCCT
Ppargc1a	NM_008904.2	CCCAGAGTCACCAAATGACCCCA	CCTCTTGGTTGGCGGTGGCA
Rplp0	NM_007475	TCTGGAGGGTGTCCGCAACG	GCCAGGACGCGCTTGTACCC
Ly6a/Sca1	NM_001271416.1	TGCCCATCAATTACCTGCCC	TTGAGAATCCACAATAACTGCTGC
Scd1	NM_009127.4	GCTCTACACCTGCCTCTTCGGGAT	TCCAGAGGCGATGAGCCCCG
Tbx1	NM_011532.2	CAAGGCAGGCAGACGAATGT	TACCGGTAGCGCTTGTCATC
Tgfb1	NM_011577	GCTGAACCAAGGAGACGGAA	ATGTCATGGATGGTGCCCAG
Tnf	NM_013693	GTCCCCAAAGGGATGAGAAG	CACTTGGTGGTTTGCTACGA
Tnfrsf9	NM_011612.2	GGAGCTAACGAAGCAGGGTT	CGTCTAGAGAGCAGTTCGTCC
Ucp1	NM_009463	TCAGGATTGGCCTCTACGAC	TGCATTCTGACCTTCACGAC

Dataset S1. NF-κB-targeted genes regulated by sMR.
https://www.pnas.org/doi/suppl/10.1073/pnas.2103304118/suppl_file/pnas.2103304118.sd01.xlsx

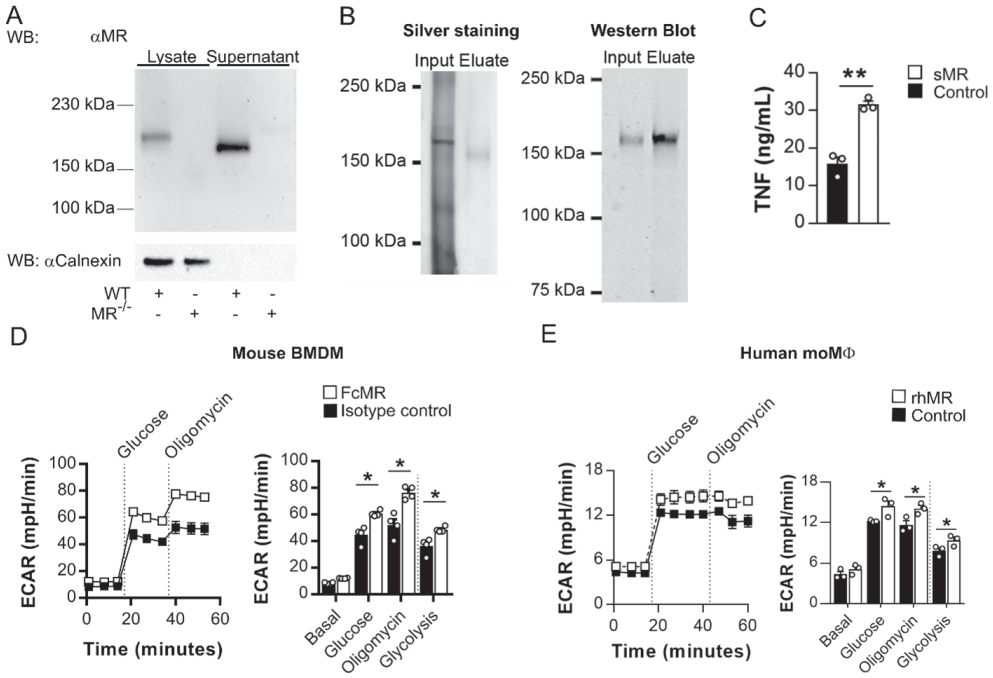

Supplementary Figure 1. Purification of sMR from the supernatant of MR-expressing cells and its effect on cytokine secretion. (**A**) The presence of the MR in the cell lysates or supernatant from wild-type or MR-deficient macrophages was determined by Western blot. (**B**) sMR was purified by affinity chromatography using a Protein A/G column covalently linked to an MR-specific antibody. Images depict silver staining (left) and Western blot using a MR-specific antibody (right). (**C**) MR-deficient macrophages were treated with purified sMR (30 ng/mL) and stimulated with LPS. Secretion of TNF was determined after 18 h by ELISA. (**D-E**) Real-time glycolysis in FcMR or isotype control-treated mouse macrophages (*D*) or recombinant human MR-treated human monocyte-derived macrophages (*E*) as measured through extracellular acidification rate (ECAR). Cells were pre-incubated in glucose-free medium (basal), followed by sequential addition of glucose and oligomycin. Glycolysis is calculated as the increase in ECAR in response to glucose ([ECAR Glucose] – [ECAR Basal]). All graphs are depicted as mean ± SEM; for all experiments, n ≥ 3. **P* <0.05.

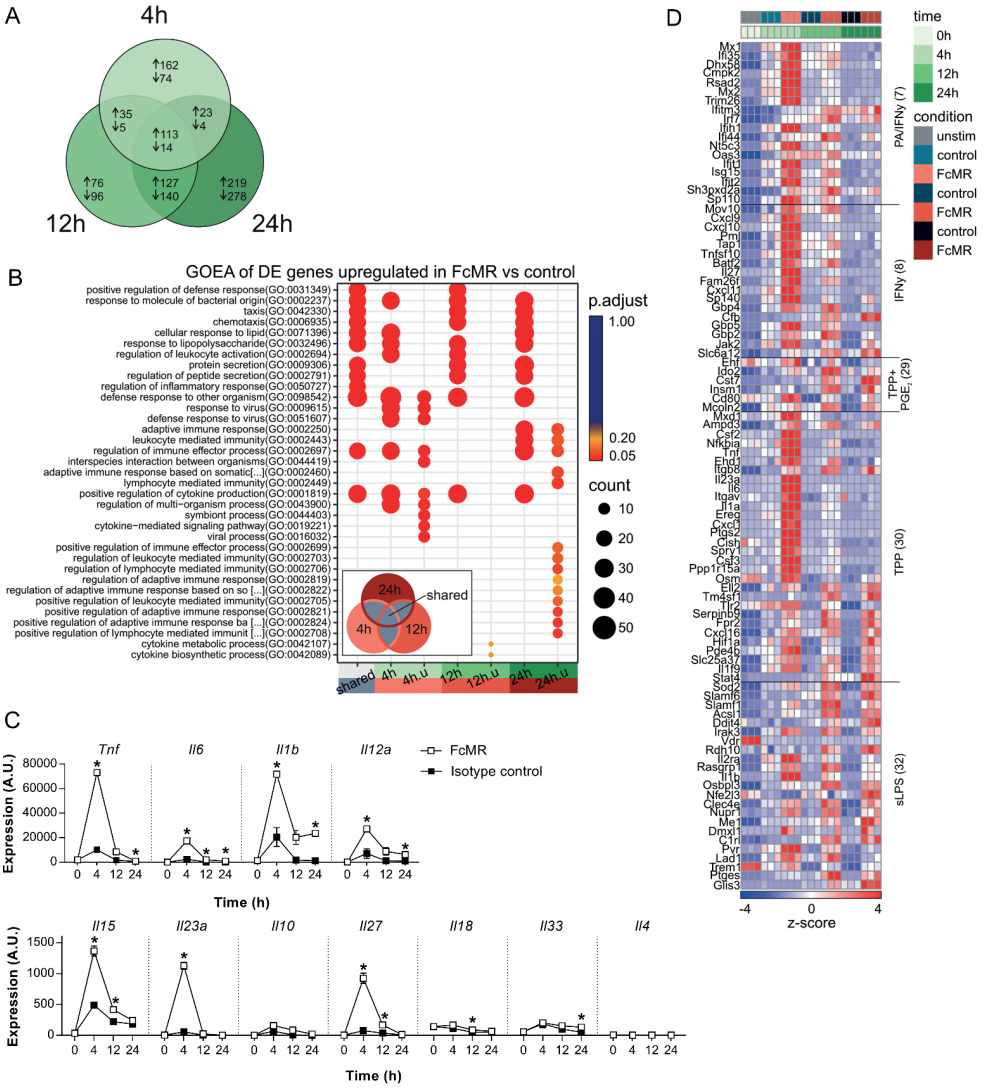

Supplementary Figure 2. RNAseq analysis of bone marrow-derived macrophages incubated with FcMR or isotype control for 4, 12, or 24h. (**A**) Venn diagram of 1,366 DE genes in FcMR-treated versus control samples. (**B**) Dot plot of gene ontology enrichment analysis (GOEA) results of the DE genes shared between all three DE gene sets (shared), the respective DE gene sets for each time point (4 h, 12 h, and 24 h) and those DE genes unique for each time point (4 h.u, 12 h.u, and 24 h.u). (**C**) Expression of indicated cytokines after treatment with FcMR or isotype control as measured by RNAseq. (**D**) Heatmap of hierarchically clustered, normalized and z-scaled expression values of the genes corresponding to the enriched stimulus-specific macrophage expression signatures shown in Figure 2E. *P <0.05.

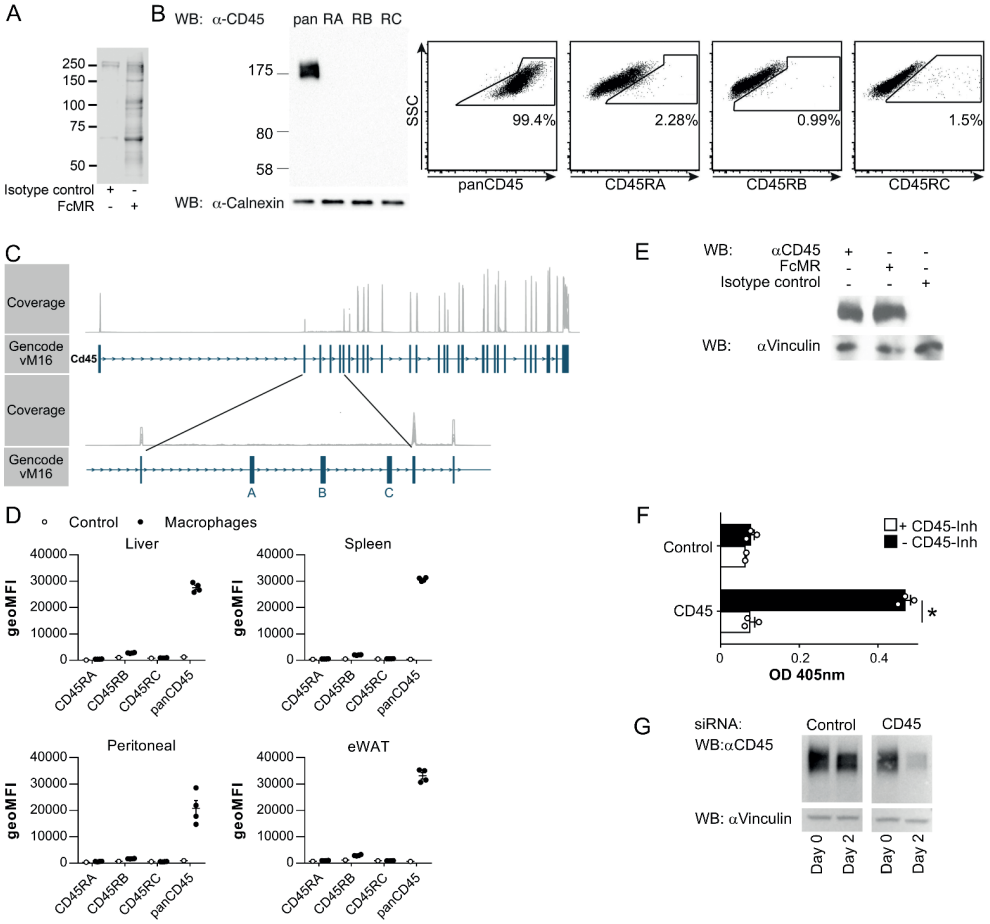

Supplementary Figure 3. Inhibition of CD45 by the MR. (**A**) Lysates from surface biotinylated macrophages were immune precipitated with FcMR or isotype control and analyzed by Western blot using neutravidin. (**B**) CD45 isoforms on bone marrow-derived macrophages (BMDMs) analyzed by Western blot and flow cytometry. (**C**) Visualization of the RNAseq read coverage of the murine *Cd45* locus. (**D**) Analysis of CD45 isoforms on macrophages from spleen, liver, white adipose tissue (WAT) and the peritoneal cavity (PEC) by flow cytometry. Open circles indicate fluorescence minus one (FMO) controls. (**E**) F4/80^{+} splenic macrophages were isolated by magnetic separation. Cell lysates were analyzed by far Western blot after staining with FcMR or isotype control or by Western blot with antibodies against CD45 and vinculin. (**F**) CD45 was immune precipitated from cell lysates from BMDMs and incubated with 4-NPP in the presence or absence of the CD45 inhibitor SF1670. Graph depicts dephosphorylation of 4-NPP. Samples without CD45 antibody were used as controls. (**G**) siRNA-mediated down-regulation of CD45. All graphs are depicted as mean ± SEM; for all experiments, n ≥ 3. *P <0.05.

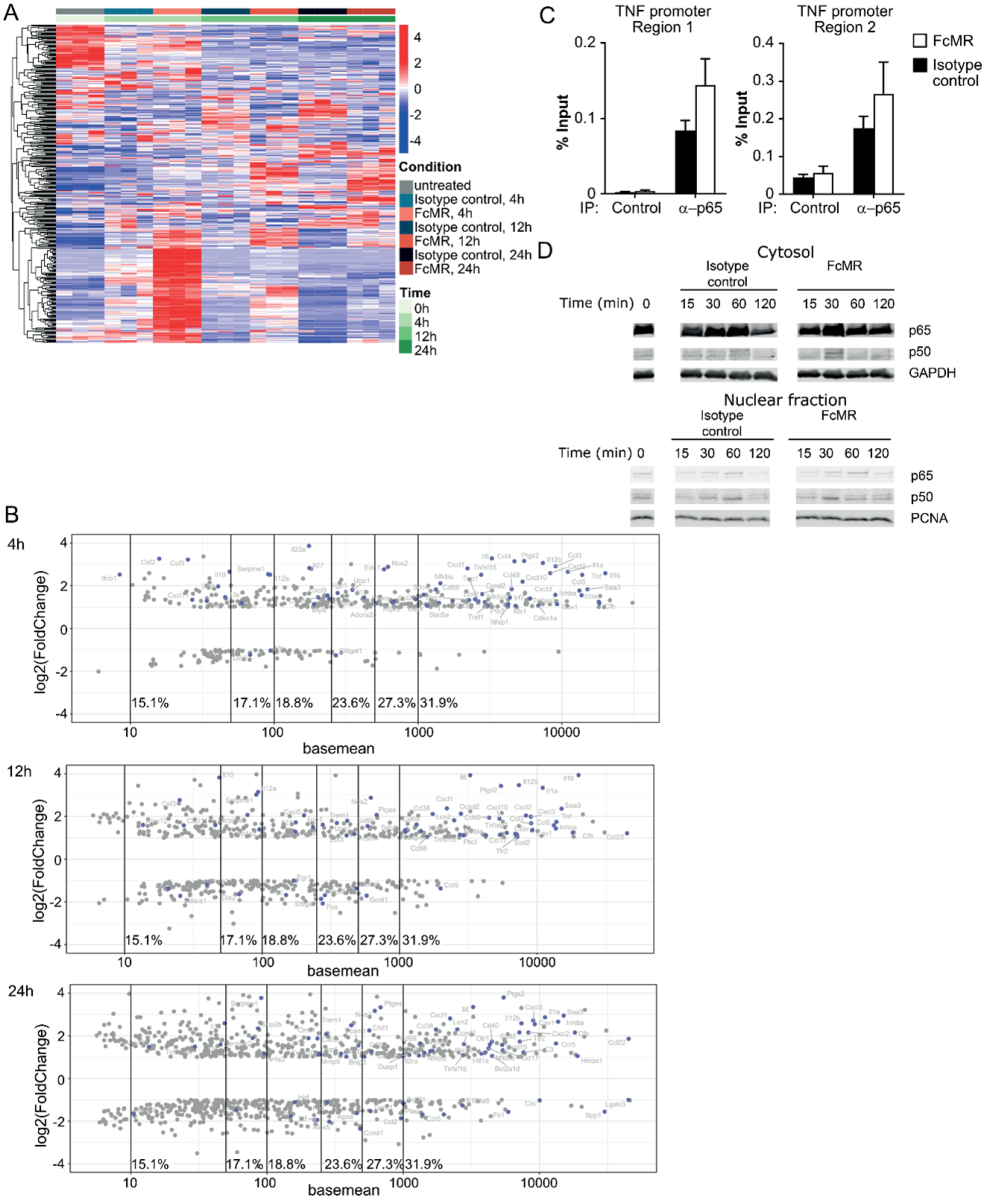

Supplementary Figure 4. Regulation of NF-κB target genes by FcMR. (**A**) Normalized and z-scaled expression values of 351 NF-κB target genes present in our data set across time and treatments. 118 genes were significantly differentially expressed at least one time point comparing the FcMR-treated cells with controls. (**B**) MA plots showing fold changes and mean expression values (BaseMean) of significantly differentially expressed genes comparing the FcMR-treated cells with controls at the respective time point. Blue dots indicate NF-κB target genes. Numbers indicate the percentage of NF-κB target genes amongst all

◀Supplementary Figure 4. Legend (Continued)

DE genes that display a BaseMean value of at least 10, 50, 100, 250, 500, or 1,000. (**C**) BMDMs were incubated with FcMR or isotype control for 60 min. Recruitment of p65 towards the TNF promoter was monitored by ChIP. (**D**) MR-deficient macrophages were incubated with FcMR or isotype control in the presence of the Akt inhibitor MK-2206 (5 mM). p65 and p50 were determined in the cytosolic and nuclear fraction by Western Blot.

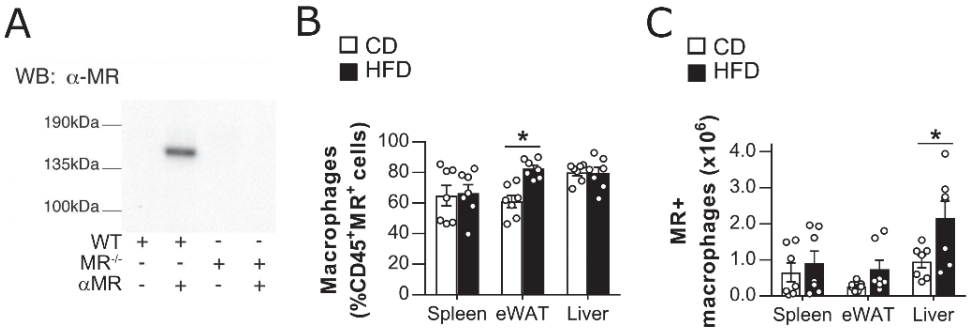

Supplementary Figure 5. MR serum levels and numbers of MR expressing macrophages in metabolic tissues during obesity. (**A**) sMR serum levels from wild-type or MR-deficient mice and depicted by Western blot. (**B**) Percentage of $F4/80^+CD64^+$ macrophages within $CD45^+MR^+$ cells in indicated tissues of HFD or CD-fed mice. (**C**) Absolute numbers of $MR^+F4/80^+CD64^+$ macrophages in the indicated tissues. All graphs are depicted as mean ± SEM; n = 6-7 per group. $^*P < 0.05$.

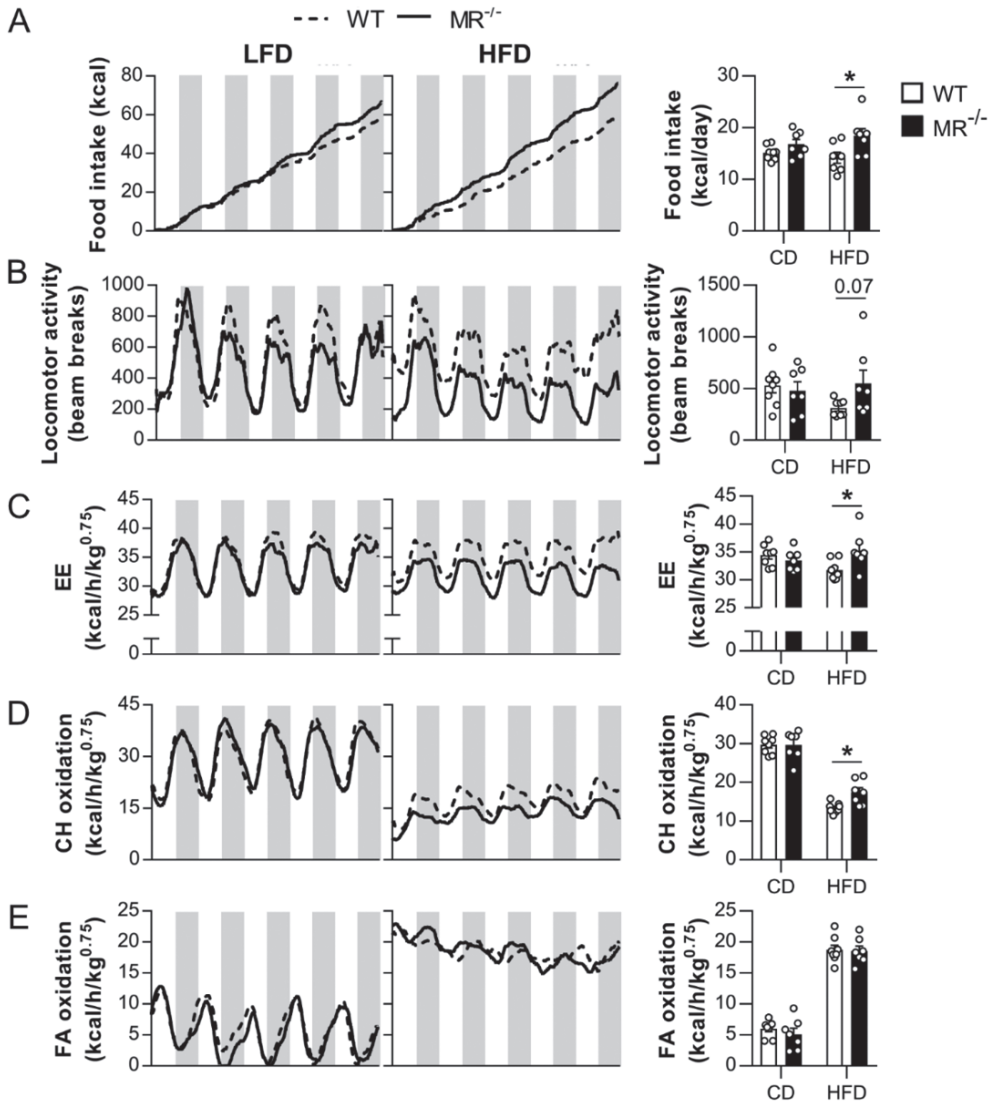

Supplementary Figure 6. MR deficiency counteracts HFD-induced decrease in locomotor activity, whole-body energy expenditure, and carbohydrate oxidation. (**A-E**) Wild-type (WT) and MR-deficient (MR$^{-/-}$) mice were fed either CD or HFD. At week 16, mice were subjected to individual indirect calorimetric measurements using fully automated metabolic cages with free access to food and water. After 48 h acclimatization, cumulative food intake (*A*), spontaneous locomotor activity (*B*), energy expenditure (EE; *C*), carbohydrate (CH; *D*) and fatty acid (FA; *E*) oxidation were measured for 5 consecutive days (white part = light phase; grey part = dark phase). The daily averages for each of the abovementioned parameters were calculated. Results are expressed as means ± SEM; n = 6-8 mice per group. *P <0.05.

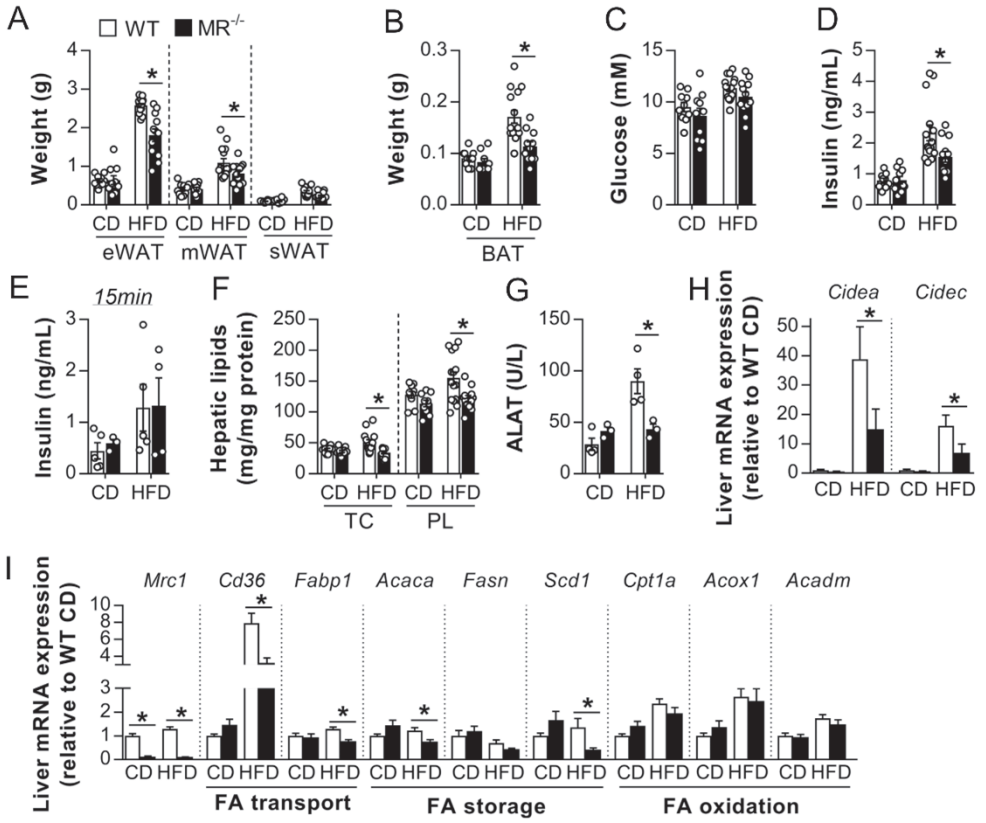

Supplementary Figure 7. MR regulates whole-body metabolic homeostasis. Wild-type and MR$^{-/-}$ mice were fed a CD or HFD for 18 weeks. (**A**) Weight of different white fat pads. (**B**) Weight of intrascapular brown adipose tissue. (**C-D**) Fasting blood glucose and plasma insulin levels. (**E**) Plasma insulin levels at 15 minutes post glucose injection during GTT. (**F**) Liver triglycerides (TG) and phospholipids (PL). (**G**) The plasma concentrations of alanine aminotransferase (ALAT) in pooled samples of 2-3 mice from two separate experiments (3-4 pooled samples per group). (**H**) Hepatic expression of the indicated genes. (**I**) Hepatic expression of the indicated genes. All the RT-qPCR results are expressed as relative to the housekeeping gene *Rplp0* (RPLP0/36B4) as fold change vs WT-CD mice. Results are expressed as means ± SEM; n = 9-16 mice per group, except for E (n = 3-5 per group), G (n = 3-4 mice per group) and H (n = 5 mice per group). **P* <0.05.

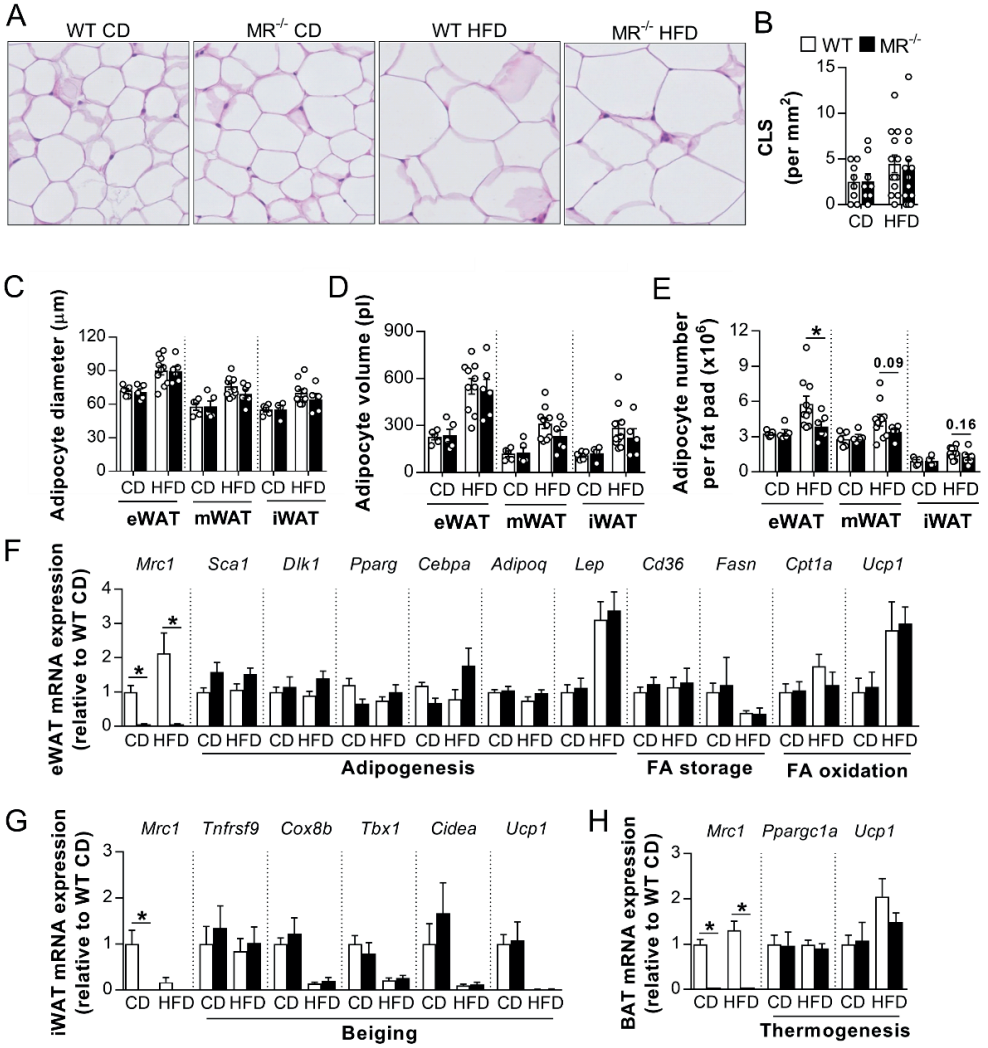

Supplementary Figure 8. MR deficiency did not affect adipocyte hypertrophy, brown adipose tissue thermogenesis, and white adipose tissue beiging. (**A-B**) Wild-type and MR-deficient mice were fed either CD or HFD for 18 weeks. At sacrifice, epididymal white adipose tissues (eWAT) were collected (*A*) and crown-like structures (*B*) were determined. (**C-E**) Adipocyte diameter (*C*), volume (*D*) and number (*E*) per fat pad were determined in eWAT, mesenteric (mWAT) and inguinal adipose tissues (iWAT). (**F**) The mRNA expression of *Mrc1* (MR) and indicated key genes involved in adipocyte physiology were measured by RT-qPCR in eWAT. (**G-H**) The mRNA expression of *Mrc1* and thermogenic (*G*) or beiging (*H*) markers were measured by RT-qPCR in iWAT and BAT, respectively. All the RT-qPCR results are expressed as relative to the housekeeping gene *Rplp0* (RPLP0/36B4) as fold change vs WT-CD mice. Results are expressed as means ± SEM. n = 10-15 mice per group. **P* <0.05.

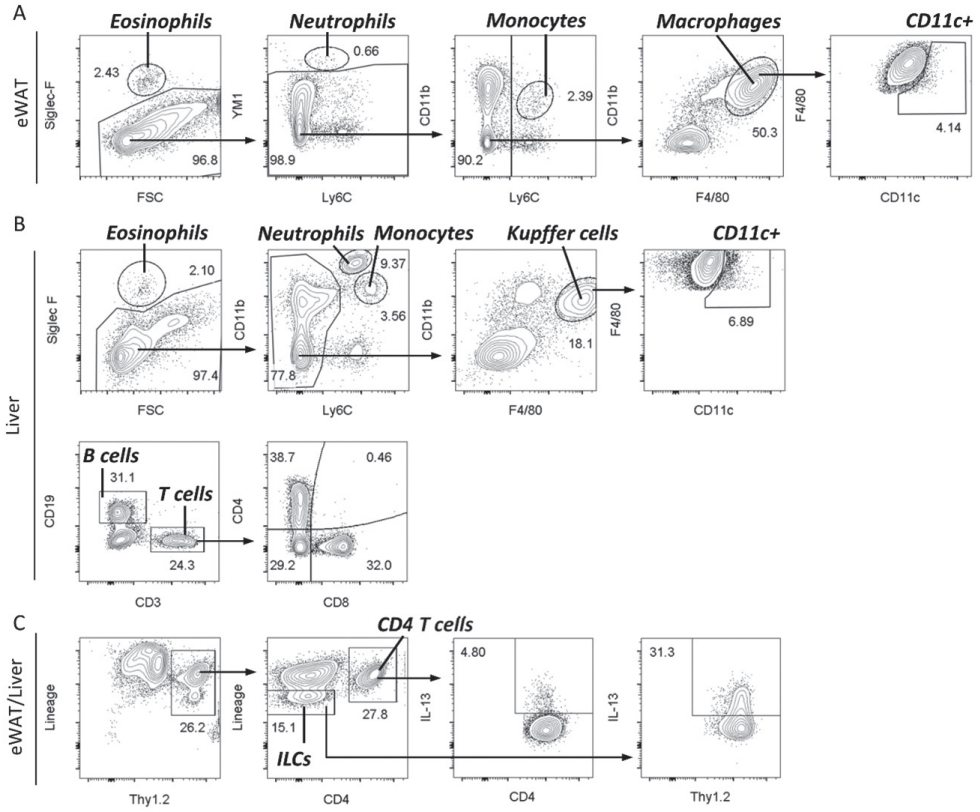

Supplementary Figure 9. Gating strategies. (**A-B**) Gating strategies for indicated cell populations in eWAT (*A*) and liver (*B*). Cells were pre-gated on live, singlet, CD45+ cells. (**C**) Gating strategy for identification of Th2 cells (IL-13$^+$ CD4 T cells) and ILC2s (IL-13$^+$ ILCs) after *ex vivo* restimulation with PMA, ionomycin and Brefeldin A. Example is shown for eWAT sample, but gating strategy is similar for liver samples.

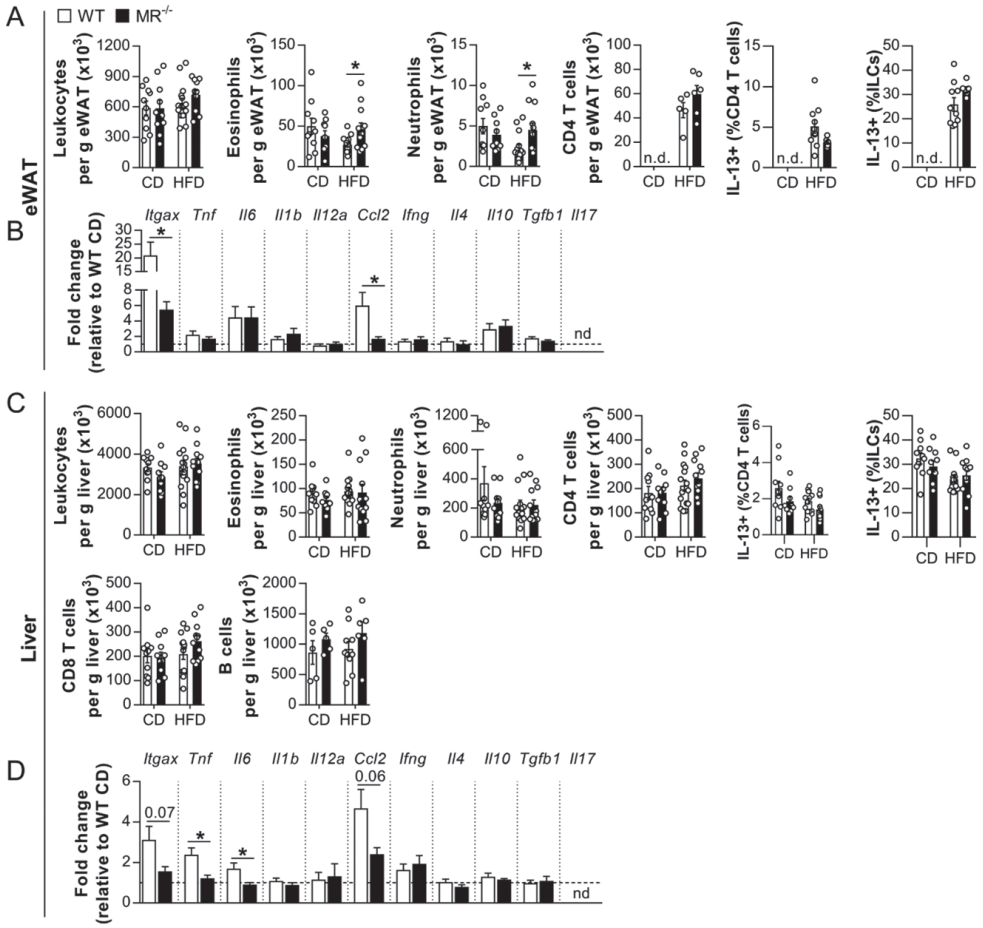

Supplementary Figure 10. Effect of MR deficiency on metabolic tissue immune cells. Wild-type and MR-deficient mice were fed either CD or HFD for 18 weeks. (**A**) Numbers of leukocytes, eosinophils, neutrophils and CD4 T cells per gram tissue, and percentages of IL-13$^+$ CD4 T cells and ILCs in eWAT. (**B**) mRNA expression levels of selected cytokines and activation markers in eWAT after 18 weeks on HFD monitored by RT-qPCR. (**C**) Numbers of leukocytes, eosinophils, neutrophils, CD4 T cells, CD8 T cells and B cells per gram tissue, and percentages of IL-13$^+$ CD4 T cells and ILCs in liver. (**D**) mRNA expression levels of selected cytokines and activation markers in liver after 18 weeks on HFD. All the RT-qPCR results are expressed as relative to the housekeeping gene *Rplp0* (RPLP0/36B4) as fold change vs WT-CD mice. Gating strategies are shown in Supplementary Figure 9. Results are depicted as means ± SEM; n = 10-15 mice per group for all, except eWAT CD4 T cells (n = 5-6 mice per group). *P <0.05.

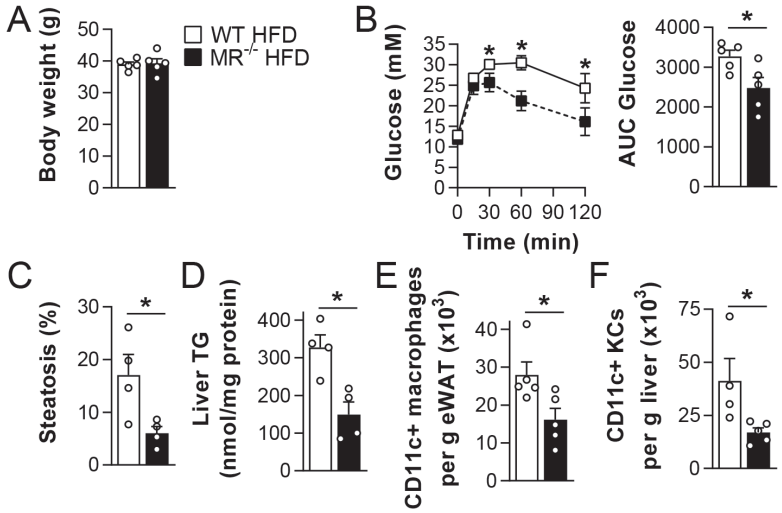

Supplementary Figure 11. MR regulates whole-body metabolic homeostasis and proinflammatory activation of metabolic tissue macrophages independently of changes in body weight in obese mice. (**A**) Wild-type and MR-deficient mice were matched on body weight after 18 weeks on HFD. (**B**) At week 17, an intraperitoneal glucose tolerance test was performed. (**C**) After sacrifice, hepatic steatosis was quantified from H&E-stained slides. (**D**) Liver TG content was measured. (**E-F**) The numbers of CD11c^{+} macrophages were determined in eWAT (*E*) and liver (*F*). Results are expressed as means ± SEM; (n = 4-5 mice per group). **P* <0.05.

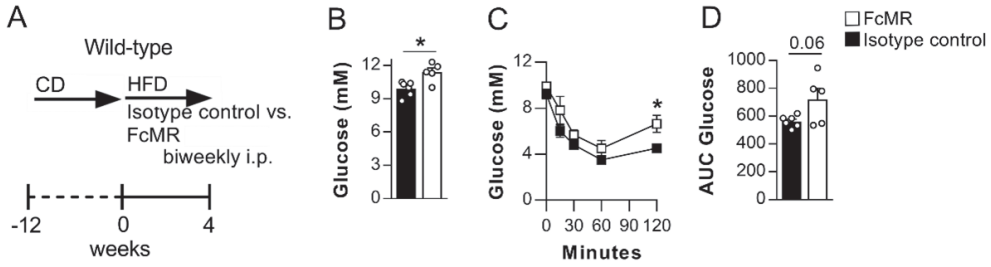

Supplementary Figure 12. sMR treatment regulates whole-body metabolism in HFD-fed mice. (**A**) Wild-type mice were fed a HFD and concomitantly injected i.p. with 4.82 mmoles/mouse FcMR or isotype control every 3 days. (**B-D**) After 4 weeks, fasting blood glucose levels were measured (*B*) and an intraperitoneal insulin tolerance test (*C, D*) was performed. Results are expressed as means ± SEM; n = 6 mice per group. **P* <0.05.